



Research Article


Calibration of κ - ϵ turbulence model for thermal–hydraulic analyses in rib-roughened narrow rectangular channels using genetic algorithm



Abid Hossain Khan¹  · Md.Shafiqul Islam² · Istiak Uddin Sazzad²

Received: 27 October 2020 / Accepted: 5 May 2021

Published online: 30 May 2021

© The Author(s) 2021 

Abstract

Nowadays, applications of turbulent fluid flow in removing high heat flux in rib-roughened narrow channels are drawing much interest. In this work, an improved version of the κ - ϵ turbulence model is proposed for better prediction of thermal–hydraulic characteristics of flow inside rib-roughened (pitch-to-rib height (p/k) ratio = 10 and 20) narrow channels (channel height, $H = 1.2$ mm and 3.2 mm). For this, the four turbulence model parameters, C_{μ} , $C_{\epsilon 1}$, $C_{\epsilon 2}$, and σ_k are calibrated. These parameters are adjustable empirical constants provided for controlling the accuracy of the turbulence model results when needed. The simulated data are used to develop correlations between the relative errors in predicting the friction factor (f), Nusselt number (Nu), and the model parameters using a multivariate nonlinear regression method. These correlations are used to optimize the errors using genetic algorithm. Results reveal that the calibrated parameters are not the same for all the narrow channel configurations. After calibration, the overall predictive improvements are up to 35.83% and 27.30% for $p/k = 10$ and $p/k = 20$ respectively when $H = 1.2$ mm. Also, up to 15.48% and 18.05% improvements are obtained for $p/k = 10$ and $p/k = 20$ respectively when $H = 3.2$ mm. The role of the two parameters $C_{\epsilon 1}$ and $C_{\epsilon 2}$ are found to be of primary importance. Furthermore, three types of nanofluids i.e. Al_2O_3 -water, CuO-water, and TiO_2 -water are studied using the calibrated model to check the potentiality of heat transfer enhancement. Among them, CuO-water nanofluid is predicted to have around 1.32 times higher value of Nu than pure water for the same narrow channel configuration.

Article Highlights

- κ - ϵ turbulence model is calibrated for rib-roughened narrow rectangular channels using genetic algorithm.
- $C_{\epsilon 1}$ and $C_{\epsilon 2}$ are the most influential parameters on the performance of the model inside rib-roughened narrow channel.
- Suggested calibration process is more effective for channel height of 1.2 mm than 3.2 mm.

Keywords Rib-roughened narrow channel · Computational fluid dynamics · Heat transfer enhancement · Turbulence model · Genetic algorithm

✉ Abid Hossain Khan, khanabidhossain@gmail.com; Md.Shafiqul Islam, msislam@du.ac.bd; Istiak Uddin Sazzad, istiaksazzad@gmail.com | ¹Institute of Nuclear Power Engineering, Bangladesh University of Engineering and Technology, Dhaka 1000, Bangladesh. ²Department of Nuclear Engineering, University of Dhaka, Dhaka 1000, Bangladesh.



SN Applied Sciences

(2021) 3:678

| <https://doi.org/10.1007/s42452-021-04645-x>

Abbreviations

Symbols

CFD	Computational fluid dynamics
GA	Genetic algorithm
MSE	Mean squared error

Greek Symbols

κ	Turbulence kinetic energy (J/kg)
\emptyset	Volume fraction
μ	Dynamic viscosity (kg/m.s)
ρ	Density (kg/m ³)
ε	Turbulence dissipation rate
\in	Relative error

Vectors

\dot{E}	Rate of energy transfer
\mathbf{F}	Force
\mathbf{I}	Inertia tensor
$\dot{\mathbf{q}}$	Heat flux
\mathbf{u}	Velocity

Symbols

C_p	Specific heat (J/kg.K)
f	Friction factor
F_v	Fitness value
k_T	Thermal conductivity (W/m.K)
\dot{m}	Mass flow rate (kg/s)
Nu	Nusselt number
P_w	Wetted parameter (m)
P	Pressure (Pa)
Pr	Prandtl number
\dot{Q}	Rate of heat transfer (W)
Re	Reynolds number
T	Temperature (°C)
v	Velocity (m/s)
$C_{\mu}, C_{\varepsilon 1}, C_{\varepsilon 2}, \sigma_k, \sigma_\varepsilon$	k - ε Turbulence model parameters

Subscripts

bf	Base fluid
nf	Nanofluid
s	Solid particle

1 Introduction

Micro-channel and mini-channel heat sinks are the core components of modern heat removal technology. With the advancement of technology, the size of a modern machine/device has reduced significantly while their functionality has remained unchanged. As a result, efficient heat removal techniques have become more challenging issues than ever. Micro-channel and mini-channel heat sinks are the most lucrative options. Due to their superior heat transfer performances, they have widespread use in

high-performance computer chips, diodes, nuclear fission and fusion reactors, etc. where a high heat removal rate is required in the order of 10^2 – 10^4 W/cm² [1]. In most cases, the micro-channel and mini-channel heat sinks have their surfaces roughened with ribs (also called turbulence promoters) of various shapes and sizes. These ribs are provided to increase the heat transfer surface area as well as to destabilize the growth of boundary layers. Although micro-channel or mini-channel heat sink with a rib-roughened surface ensures better heat transfer performances with the expenses of pressure drop, it is difficult to accurately predict the fluid flow and heat transfer mechanisms. This is because the conventional correlations for predicting the friction factor and convective heat transfer coefficient through smooth narrow channels are not applicable for rib-roughened channels. Heat transfer enhancement in micro/mini-channels with rib-roughened surfaces in the turbulent flow regime creates a high pressure drop. That requires a higher pumping power. For this, costly experimental setups are required to evaluate the exact heat transfer and fluid flow mechanism through rib-roughened narrow channels of various shapes, sizes and rib configurations. Han et al. [2] conducted study on heat transfer augmentation on rectangular narrow channels with rib turbulators. Islam et al. [3] conducted a similar study on rectangular narrow channels with square micro-ribs. He later extended the work to analyze the influence of turbulence flow structure on the enhancement of heat transfer in those channels [4, 5]. Chang, Liou and Lu [6] studied heat transfer enhancement in narrow rectangular channel with two opposite rib-roughened walls. The work was extended to observe the effect for skewed ribs [7]. Esmaili, Ranjbar and Porkhail [8] conducted experimental analysis on heat transfer in ribbed microchannels. Ma et al. [9] performed a comparative study with steam and air for convective heat transfer performance inside a rib-roughened channel.

Nowadays computation methods are so powerful that they predict very close to experiments. Many researchers apply Computational Fluid Dynamics (CFD) modeling tool for analyzing the fluid flow and heat transfer characteristics in rib-roughened narrow channels and validate with experimental data. Moon, Park and Kim [10] evaluated heat transfer performance for various rib shapes. Mereu, Lampitella and Inzoli [11] conducted CFD analysis for both flat and ribbed square ducts. Khan, Kim and Kim [12] studied the performance of various rib configurations for microchannel heat sinks. Moon and Kim [13] attempted to optimize of a rotating equilateral triangular cooling channel with staggered square ribs. Khalid, Xie and Sunden [14] performed a CFD-based study to observe the flow structure and heat transfer in a square ribbed channel with varying rib pitch ratio. The CFD-approach is well-suited for

laminar flow analysis even for complex shapes and geometries of the flow channels or surfaces. This is, however, not the case for turbulent flow analysis. Also, for the turbulent flow case, there are no empirical correlations available to predict the fluid flow and heat transfer behaviors. Instead, various turbulence models were proposed by researchers to predict turbulence flow characteristics [15]. In many cases, it is observed that the results from a specific turbulence model do not agree well with experimental results. In this field of interest, there are no such studies available in the literature except for a few, such as of Islam et al. [3].

Islam et al. [3] conducted experiments on heat transfer augmentation in rib-roughened narrow channels where water is used as the coolant. The rib pitch-to-height ratios (p/k) were 10 and 20 with a constant rib height (k) of 0.2 mm. Reynolds number (Re) was varied in the range 2,400–98,500 at channel heights (H) of 1.2 mm and 3.2 mm. The results revealed that the heat transfer can be increased 2–2.5 times in a turbulent flow regime by introducing the ribs on one side of the surface of the channel under constant heat flux condition. The values of Nusselt numbers (Nu) were, however, slightly lower than that predicted by correlations from the available literature. On the other hand, the values of friction factors (f) from experiments were found to be much lower than the predicted values using correlations by Webb et al. Subsequently, new correlations for calculating f and Nu were derived for these rib-roughened narrow channel configurations [3]. This work was extended later on by the same authors to predict the turbulence flow structure over the rib-roughened surface using a particle image velocimetry technique [4] to detect the heat transfer enhancement mechanism. The stream-wise mean velocity and turbulent kinetic energy distributions at different locations for the $Re=7,000$ and 20,000 were obtained. The values were also compared with the predicted values by the standard κ - ϵ and non-linear κ - ϵ turbulent models [5]. Results revealed that both the turbulence models failed to predict accurately the flow characteristics over the rib-roughened surface. This resulted in both the models predicting unusually high frictional factors for turbulent flow in narrow channels. However, the study did not provide a possible solution to overcome the limitations. Also, the study didn't explore the prospect of using other fluids with better heat transfer properties such as nanofluids.

In such a situation, it is necessary to calibrate the turbulence model parameters so that it can be employed to analyze a specific flow condition. In this work, the authors first attempt to find the suitability of the standard κ - ϵ turbulence model in predicting the thermal-hydraulic characteristics of a rib-roughened narrow channel similar to the experiments by Islam et al. Then attempts are made to calibrate the four turbulence model parameters, C_{μ} , $C_{\epsilon 1}$,

$C_{\epsilon 2}$ and σ_k to improve the standard κ - ϵ turbulence model. A new approach for the calibration process is suggested that combines multivariate nonlinear regression analysis and genetic algorithm (GA) for error minimization. A comparative study is conducted between the default and calibrated values of the turbulence model parameters to determine which set of values ensure better prediction of κ - ϵ turbulence model in this specific application. After fixing the improved κ - ϵ turbulence model, the three different nanofluids, i.e. Al_2O_3 -water, CuO -water, and TiO_2 -water, are introduced in the narrow channels to predict the enhanced heat transfer rates with regards to pure water. This paper is organized in five sections, starting with a brief introduction in Sect. 1, literature survey and identification of research gap in Sect. 2, methodology of this study in Sect. 3, results and discussion are presented in Sect. 4 and concluding remarks in Sect. 5 at the end of the paper.

2 Studies of heat transfer enhancement in mini/ micro-channels

For the past few years, numerous studies were conducted to understand the effect of micro-ribs on the thermal-hydraulic characteristics of narrow channel flow. Ali, Tariq and Gandhi [16] studied the effect of the chamfering angle on the heat transfer augmentation for flow through a slit with surface-mounted triangular ribs. Seo, Afzal and Kim [17] performed a multi-objective optimization of a boot-shaped rib in a cooling channel. Popov, Skrypnik and Schelchkov [18] studied heat transfer and pressure drop in pipes with inner helical micro-ribs. Wang, Qian and Ding [19] studied the improvement in laminar flow heat transfer in micro-channels where bilateral rib was used instead of vertical or span-wise ribs. Results from the study revealed that the Nu of the micro-channel with bilateral ribs was higher than those of micro-channels with vertical ribs and span-wise ribs. Li et al. [20] experimentally investigated the heat transfer and flow characteristics of micro-channels with micro-ribs. In his work, the thermal performance index of a micro-channel with one-sided ribs was found to be higher than those of the micro-channels with no ribs and both-sided ribs. Fadhil, Al-Turaihi and Abed [21] studied the effect of semi-circular ribs on the heat transfer coefficient in a rectangular channel. Ali, Sharma and Tariq [22] studied the performance of trapezoidal ribs of various taper angles. Li et al. [23] investigated turbulent flow in a rotating straight channel with continuous ribs. Results revealed that rotation changed the turbulence flow characteristics significantly.

In recent times, nanofluids have emerged as potential candidates for various heat transfer applications. Numerous studies were conducted to study the behavior

of nanofluids while flowing through a narrow channel. Akbari et al. [24] studied the effect of rib height on the heat transfer and flow parameters of water- Al_2O_3 nanofluid. Alipouret al. [25] numerically investigated the influence of T-semi attached ribs on turbulence flow and heat transfer parameters of silver-water nanofluid. Behnampour et al. [26] analyzed the heat transfer and flow characteristics of silver-water nanofluid in micro-channels with trapezoidal, rectangular, and triangular ribs. The study found triangular ribs to be the best performing one in a laminar flow regime. Gravndyan et al. [27] studied the effect of rib aspect ratio on the heat transfer and laminar flow characteristics of water-TiO₂ nanofluid in rectangular micro-channel. Results revealed that the f was independent of the aspect ratio of rib but is dependent on the volume fraction of nanoparticles. Shamsi et al. [28] investigated the increase in heat transfer in a rectangular micro-channel with triangular ribs for water-CMC nanofluid. The study proposed that a triangular channel with 30° attack angle has the biggest Nu and pressure drop along the channel provided that the flow is laminar. Gholami et al. [29] studied the effect of rib shape on the laminar flow behavior of oil-MWCNT nanofluid in rectangular micro-channel. The work found a parabolic rib as the best performing one in terms of Nu enhancement. Parsaiemehr et al. [30] studied turbulence flow and heat transfer of water- Al_2O_3 nanofluid in a rectangular channel. Cheloi, Akbari and Toghraie [31] utilized CFD to investigate the laminar flow heat transfer of water-Cu nanofluid inside a ribbed rectangular micro-channel. Pahlevaninejad, Rahimi and Gorzin [32] studied the thermal-hydraulic behavior of water- Al_2O_3 nanofluid while flowing through a wavy micro-channel with rectangular obstacles.

As mentioned earlier, the CFD results employing the standard turbulence models do not converge with experimental results when the geometry is too complex. In those cases, improvements or calibrations of the turbulence model employed are necessary. There are various works related to the calibration of a specific turbulence model. Rocha et al. [33] performed calibration of κ - ω SST turbulence model for analyzing flow over a small-scale horizontal axis wind turbine. The study reported that the value of β^* significantly affects the accuracy in predicting viscous friction over the blades. The work was later extended for wind turbine design with cambered and symmetrical airfoils [34]. Guillas, Glover and Malki-Epshtein [35] employed Bayesian calibration for the constants of κ - ϵ turbulence model to develop a CFD model of street canyon flow. Matyushenko and Garbaruk [36] calibrated κ - ω SST turbulence model for predicting the characteristics near stall-regime. The work suggested that for the value of the constant $a_1 = 0.28$, the accuracy of the model is improved significantly. DeChant et al. [37] calibrated κ - ϵ turbulence

model using an Approximate Self-similar Jet-in-Crossflow Solution. Shirzadi, Mirzaei and Naghashzadegan [38] suggested the improvement of κ - ϵ turbulence model for simulating atmospheric boundary layer around a high-rise building using stochastic optimization and Monte Carlo Sampling technique. Results revealed that an error reduction from 170 to 28% was possible for estimating the reattachment length behind the building model.

While there are many approaches for calibrating different turbulence models, all of them focus on minimizing the errors associated with the simulation process. Since error minimization is basically an optimization problem, various optimization algorithms have their potential use in the calibration process of the turbulence model. GA is one of the most extensively used nature-inspired optimization algorithms. Interestingly, a study on the use of GA for calibrating a turbulence model is not observed in the available literature. However, this algorithm was used in a wide range of heat transfer optimization problems in recent years. Liu, Bu and Xu [39] performed an optimization study of a plate-fin heat exchanger using CFD and multi-objective GA. Na et al. [40] performed a multi-objective optimization of a micro-channel reactor for Fischer-Tropsch synthesis using CFD and GA. Ghorbaniet al. [41] did a CFD modeling and optimization of a latent heat storage unit with the help of GA. Daróczyet, Janiga and Thévenin [42] optimized the shape of the airfoil geometry of an H-rotor with the help of CFD and GA. Prieler et al. [43] suggested a CFD-based optimization process for the transient heating process in a natural gas fired furnace using ANN and GA. Oh and Chein [44] demonstrated various optimization problems that may be solved by coupling CFD and GA. Sun and Yoon [45] performed multi-objective optimization of a gas cyclone separator using CFD and GA. Pourfattah et al. [46] coupled CFD and GA to optimize a vertical twisted tape arrangement in a channel subjected to MWCNT-water nanofluid.

From the literature study, it may be observed that multiple attempts were made to calibrate numerous turbulence models for getting better flow characteristics. However, to the authors' knowledge, none of the studies attempted to couple heat transfer with the flow and calibrate a turbulence model for both of them. Also, almost all of the relevant studies have dealt with gaseous fluid i.e. air. Since air and any other gaseous medium have much lower value of thermal conductivities than water and other liquid coolants, liquid coolants are preferred to gaseous coolant in many applications such as cooling channel of fusion reactors, neutron generator, target cooling of a spallation reactor, etc. where a high heat flux removal rate is required. An attempt to improve a turbulence model for predicting both heat transfer and flow characteristics of water or any other liquid medium inside a rib-roughened narrow

channel is something yet to be done. Also, introducing a GA in the calibration process of turbulence model parameters is a completely unique approach. This work, therefore, utilizes GA to improve the κ - ϵ turbulence model for analyzing the thermal-hydraulic characteristics in rib-roughened narrow channels. The work also attempts to replace ordinary water with nanofluids in these narrow channels to study the potential heat transfer enhancement rate.

3 Method

In this study, an attempt was made to improve the accuracy of κ - ϵ turbulence model in predicting the heat transfer and flow characteristics over a rib-roughened narrow channel through calibration process. Here, water was taken as the circulating flow inside the narrow channel. The CFD-based simulations were conducted in COMSOL Multiphysics 5.2b, which is a well-known commercial simulation software package. It is a multiphysics simulation software and solver based on Finite Element Analysis (FEA). The method of calibration is novel and unique in the sense that it is the first study of its kind that uses an optimization tool (here genetic algorithm) for the calibration process. Most of the works in the available literature utilized various statistical tools, but calibration through error optimization is a new approach. Also, the use of multivariate nonlinear regression analysis with multiple variables is also quite rare. Finally, this work considered improving the predictability of heat transfer and fluid flow characteristics at the same time, something that is absent in the available literature. There are three steps of the calibration process. They are:

- **Step 1** At first, random data were generated with CFD-based simulations by randomly varying the values of each turbulence model parameter.
- **Step 2** f and Nu were calculated from the data generated from the simulations and compared with established experimental correlations to find relative errors in predicting them. Separate correlations for relative errors in predicting f and Nu were developed for different geometric parameters of the narrow channel.
- **Step 3** The correlations derived in "Step 2" were used as objective functions for the multi-objective genetic algorithm for minimizing deviation of simulated f and Nu from experimental results. MATLAB codes were developed for this purpose. The values of turbulence model parameters corresponding to the minimum mean-squared errors (MSEs) were selected as the calibrated values.

After obtaining the calibrated values of the turbulence model parameters, further data were generated through CFD-based simulations to compare the results from both the calibrated model and uncalibrated model with values from experimentally developed correlations to determine the effectiveness of the calibration process. Finally, heat transfer and flow characteristics of three different nanofluids, i.e. Al_2O_3 -water, CuO -water and TiO_2 -water, were studied with the help of the improved turbulence model.

3.1 Geometry and flow considerations for computational fluid dynamics (CFD) studies

In order to improve the model, it is necessary to compare the results generated with the help of a CFD tool with related experimental results. An experimental heat transfer study on rib-roughened narrow channels with water as coolant was conducted by Islam et al. [3]. The geometric configuration of the narrow channel employed in the study is presented in Fig. 1. The study was conducted on narrow channels having one-sided heating surface length (L) 200 mm, width (W) 20 mm, and channel heights (H) 1.2 mm and 3.2 mm respectively. 25 mm of unheated lengths were kept before the inlet and after the exit of the heating surface to ensure fully developed flow over the rib-roughened surface. Micro-ribs of height (k) 0.2 mm and width (w) 0.2 mm were placed at 2 mm and 4 mm pitch (p) so that pitch-to-height ratio (p/k) was maintained as 10 and 20 respectively. The rib-roughened side of the channel was heated while the other smooth-side was kept insulated. The Re was varied in the range of 2400–98,500 to ensure turbulence flow inside the narrow channel [3]. Figure 2 presents the CAD-generated trimetric section view of the rib-roughened narrow channel for better visualization

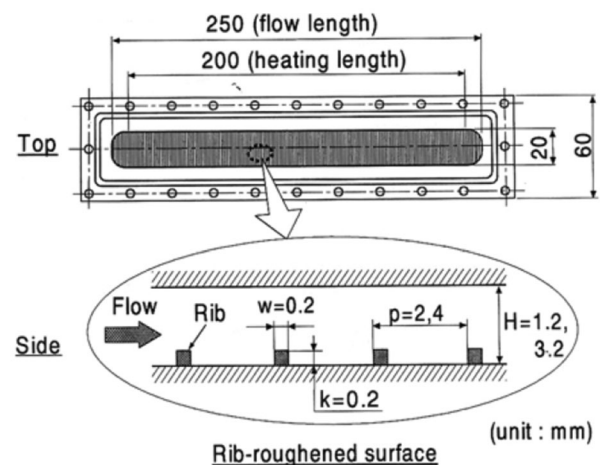


Fig. 1 The experimental setup (rib-roughened narrow channel) from the study of Islam et al. [3]

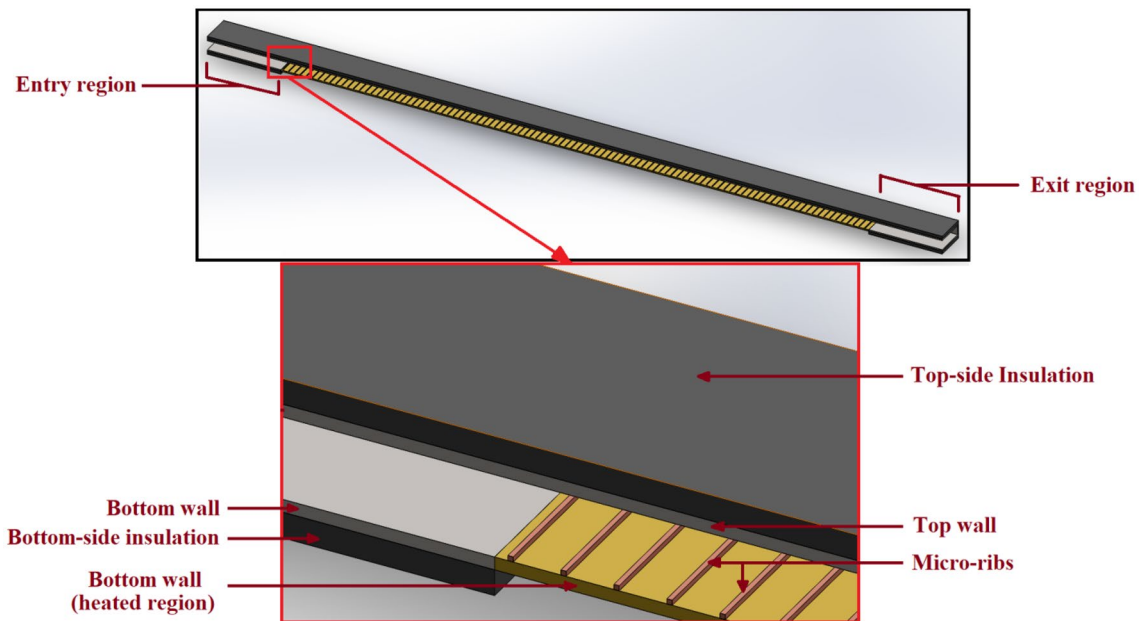


Fig. 2 Trimetric section view of the narrow channel configuration

of the channel geometry. Solidworks 2013, a CAD software, was used for this purpose.

In this numerical study, the same geometric and flow configurations were used for CFD-based simulations so that the accuracy of the turbulence model could be determined by comparing the simulation results with Islam et al.'s experimental results [3]. Since all the channels are rectangular where only one side is heated and three sides are insulated, it is more convenient to employ 2-dimensional geometries for the CFD simulations instead of 3-dimensional to reduce computation time. Although this means that the frictional losses due to the two vertical sides (not present in 2-D geometry) are neglected in the CFD simulations, the vertical sides are of much smaller width (1.2 or 3.2 mm) compared to the horizontal i.e. top and bottom sides (20 mm). Also, most of the frictional head loss should occur in the rib-roughened side i.e. bottom side of the channel, making the frictional head losses in the two side walls insignificant. Therefore, the simplification of the CFD simulation geometry should not compromise the accuracy of the results significantly. This is why the simulation geometries adopted in this study were in 2-D Cartesian coordinate system.

Two stage simulation techniques were applied;

- *Stage 1* In the first stage, a large number of sample data was generated using a commercial simulation software in order to derive correlation between the turbulence model parameters and the errors of the turbulence model in predicting the values of thermal-

hydraulic parameters i.e. f and Nu compared to the experimental results (explained in detail in Sect. 3.5). Since running simulations in full-scale geometry would consume a very large computation time, it is realistic to scale-down the simulation geometry. To do so, heating surface length was reduced from 200 to 20 mm. However, the 25 mm of unheated length at the beginning and the end (total 50 mm) were not scaled-down since the hydraulic diameter was the same for both experimental and the simulated geometry. Water inlet temperature and velocity were kept fixed at 15 °C and 5 m/s respectively and the turbulence model parameters were changed randomly for the same flow conditions (explained in Sects. 3.3 and 3.4). This allowed realizing the effect of turbulence model parameters on the accuracy of predicting outlet temperature and pressure drop of water while flowing inside the narrow channels. After that, correlations were derived using the simulated results (see Sect. 3.5). These correlations were used to find the optimum errors in calculating the f and Nu using GA (see Sect. 3.6). The turbulence model parameters corresponding to the optimized errors were taken as the calibrated values for the turbulence model.

- *Stage 2* In the second stage of CFD-based study, simulations were conducted using the calibrated values of turbulence model parameters. After obtaining the calibrated values of the turbulence model parameters, it is necessary to determine whether they significantly improve the accuracy of the simulation results or

not. To do so, CFD-based simulations were run again for both default and calibrated values of turbulence model parameters. Again, it is necessary to identify whether the amount of improvement is dependent on Re or not. To do so, the velocities of flow were varied in the range 1-15 m/s. Since number of simulations were much smaller than the previous stage and it is necessary to evaluate whether scaling down had significantly affected the calibration process or not, the CFD simulations in this stage were run in full-scale i.e. for the same geometry as the experimental setup (200 mm heated length and 50 mm insulated length). Water inlet temperature was kept fixed at 15 °C, similar to the previous stage. The simulation geometries for different stages of the study are illustrated in Figs. 3 and 4.

In the experimental study of Islam et al., there was constant heat flux throughout the heating surface [3]. However, it is well-established that Nu is a function of Re and Prandtl number (Pr) only, making the correlations equally applicable for constant temperature and constant heat flux boundary conditions [47]. Therefore, in this study, the heated surface was kept at a constant temperature of 30 °C instead of constant heat flux condition. The other side of the channel was kept insulated, similar to the experimental study. The boundary conditions are illustrated in Fig. 5.

Since there were multiple simulation geometries representing different heights and rib pitch-to-height ratios, the number of mesh elements was also different for each

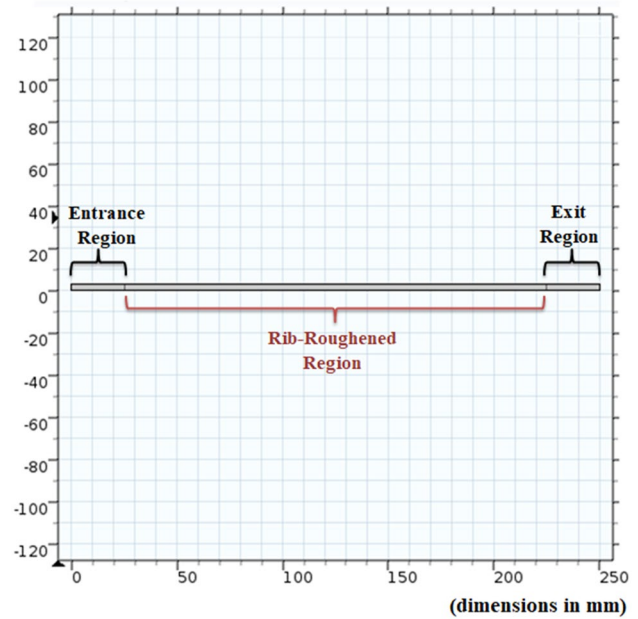


Fig. 4 CFD Simulation geometry for effectiveness analysis of the calibration process

case. In this study, default physics-controlled mesh generating option of COMSOL Multiphysics 5.2b was utilized. In order to ensure mesh independence, CFD results for the three different mesh generation options, coarse, normal, and fine, were compared. From the comparative study, it was observed that there is less than 5% variation in the results for coarse and normal meshes while there is less

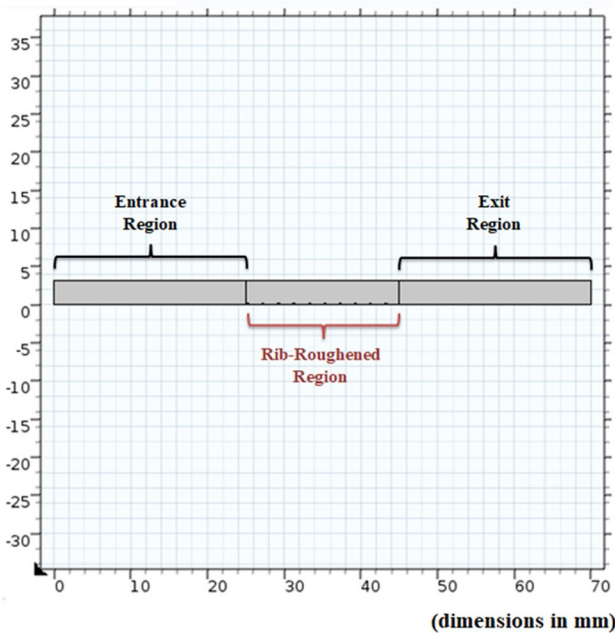


Fig. 3 CFD Simulation geometry for random data generation

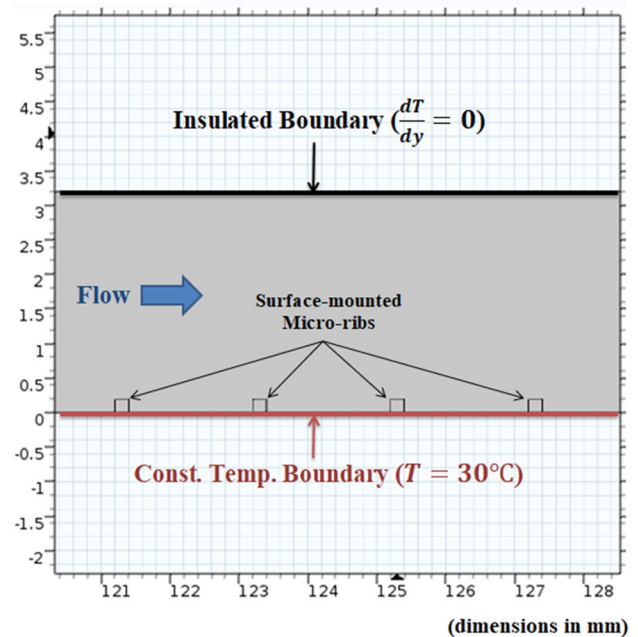


Fig. 5 Boundary conditions for simulation

than 1% variation in results for normal and fine meshes. Thus, coarse mesh was selected to reduce computation time. Also, densely meshes were generated near the ribs to fully realize the effect of turbulence eddies and flow separation. Figure 6 shows the mesh refinement near the ribs while Table 1 presents the number of mesh elements taken for each narrow channel during CFD simulation, both in reduced-scale and full-scale conditions.

3.2 Theory for thermal-hydraulic calculation

While water flows inside the narrow channel, it removes heat from the rib-roughened surface. Since water is a fluid, the mode of heat transfer in water is convection. The rate at which heat rejected by the surface is given by Eq. (1),

$$\dot{Q} = h.A_s.\Delta T_m \tag{1}$$

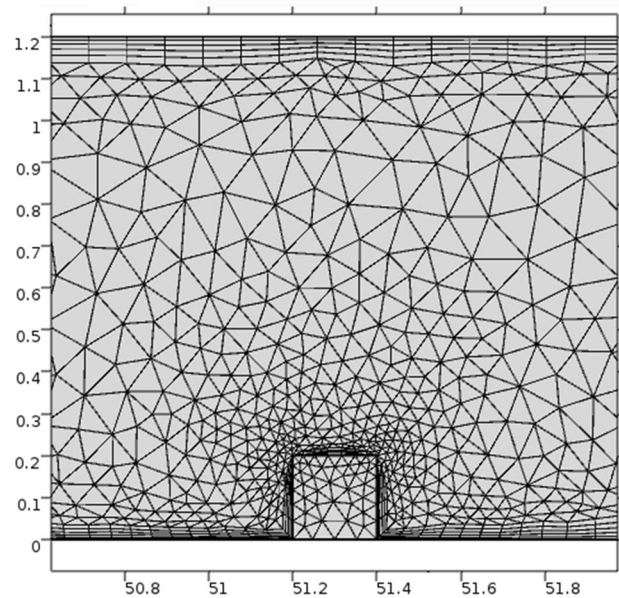


Fig. 6 Adopted different mesh sizes inside the simulated rib-roughened narrow channel

Table 1 Meshes for different simulated geometries

Geometric configuration	Reduced scale		Full-scale	
	Total element	Boundary element	Total element	Boundary element
$p/k=10, H=1.2\text{ mm}$	72,230	3405	167,364	8687
$p/k=20, H=1.2\text{ mm}$	67,471	3211	124,348	7137
$p/k=10, H=3.2\text{ mm}$	37,108	1739	155,228	6729
$p/k=20, H=3.2\text{ mm}$	33,022	1560	105,742	5131

Here, h is convection heat transfer coefficient, A_s is area of the heated surface and ΔT_m is log mean temperature difference. ΔT_m can be calculated using Eq. (2),

$$\Delta T_m = \frac{(T_{out} - T_{in})}{\ln\left(\frac{T_{wall} - T_{in}}{T_{wall} - T_{out}}\right)} \tag{2}$$

Here, T_{in} is water inlet temperature, T_{out} is exit temperature and T_{wall} is temperature of the heated surface. In this numerical study, T_{in} and T_{wall} were kept constant at 15 °C and 30 °C respectively while T_{out} was obtained from simulation. Since 2-dimensional CFD simulation geometries were adopted in this study, the outlet temperature was the line-average temperature of coolant water at the outlet boundary. This line-average value was obtained directly from the CFD tool i.e. COMSOL Multiphysics. The rate of heat transfer may also be calculated using Eq. (3),

$$\dot{Q} = \dot{m}C_p(T_{out} - T_{in}) \tag{3}$$

Here, \dot{m} is mass flow rate and C_p is specific heat of water. The mass flow rate may be calculated from Eq. (4),

$$\dot{m} = \rho vA \tag{4}$$

Here, ρ is density of water, v is velocity, and A is flow cross-sectional area of the channel. After obtaining convection heat transfer coefficient from Eq. (1), simulated Nusselt number (Nu) may be calculated using Eq. (5),

$$Nu_{sim} = \frac{hD_h}{k_T} \tag{5}$$

Here k_T is thermal conductivity of water and D_h is hydraulic diameter of the channel. Hydraulic diameter is calculated from Eq. (6),

$$D_h = \frac{4A}{p_w} \tag{6}$$

Here p_w is the wetted perimeter of the narrow channel. The simulated friction factor (f) can be obtained from Eq. (7),

$$f_{sim} = \frac{\Delta P}{2} \frac{D_h}{L_c \rho v^2} \quad (7)$$

Here, L_c is the length of the simulated channel excluding entrance and exit regions. For data generation, $L_c = 20$ mm and for validation process, $L_c = 200$ mm. Also, ΔP is pressure drop across the rib-roughened region of the channel, which was also obtained directly from simulation. Pressure drops due to the length of the entrance and exit regions were not included so that the f for only the rib-roughened region is obtained.

Equations (5) and (7) are applicable for obtaining Nu and f directly from simulation results. However, the simulation results may not always represent the actual scenario due to limitations of the flow model employed in the simulation process. To ensure accurate prediction with numerical methods, it is necessary to validate the numerical results with experimental ones or correlations derived from experimental data. If the results are not sufficiently near to experimental results, necessary calibration of the flow model is required for better output. In this study, the correlations for water-flow inside rib-roughened narrow channels were used as references to calibrate the turbulence model used for numerical data generation. The correlations for calculating the f and Nu are found in the work of Islam et al. [3].

While water is one of the most widely used heat transfer mediums till date, there are some special cooling applications where much better heat transfer characteristics is required. Nanofluids are the potential candidates for those applications. For CFD-based study with nanofluids, it is convenient for the researchers to assume that nanofluid is a single phase and homogeneous fluid [48]. This makes the correlations for determining various thermal hydraulic properties of the nanofluids such as density, thermal conductivity, specific heat, viscosity, etc. quite simplified. Akbari, Galanis and Behzadmehr [49] compared the results of the single-phase model with other two-phase models for Al₂O₃/water and Cu/water nanofluids and found that single-phase model is, despite its simplicity, more accurate. On the other hand, the work by Bianco et al. [50] found two-phase model more accurate for 100 nm Al₂O₃-water nanofluid, but the maximum difference between the average heat transfer coefficients of single-phase and two-phase model is found to be only around 11%. This study, therefore, went for single phase approach to reduce computational time and complications. The correlation for determining the viscosity of a nanofluid is given by [48],

$$\mu_{nf} = (1 + 0.025\phi + 0.015\phi^2) \mu_{bf} \quad (8)$$

Here, μ_{nf} is the viscosity of the base fluid and μ_{bf} is the viscosity of the nanofluid. Also, ϕ is the volume fraction of

the nanoparticles suspended in base fluid. In this study, $\phi = 0.02$ has been selected for the nanofluids.

Although many researchers used Eq. (8) for their CFD-based studies, the values obtained from this correlation are much lower than the experimental values for some nanofluids. Therefore, experimentally derived values of viscosities [49] for the nanofluids were used in this study.

The correlation for density is [48],

$$\rho_{nf} = (1 - \phi) \rho_{bf} + \phi \rho_s \quad (9)$$

Here, ρ_s is density of solid nanoparticle, ρ_{bf} is density of base fluid and ρ_{nf} is density of nanofluid. The correlation for specific heat is given by [48],

$$(C_p)_{nf} = \frac{(1 - \phi)(\rho C_p)_{bf} + \phi(\rho C_p)_s}{\rho_{nf}} \quad (10)$$

Finally, the correlation for thermal conductivity of the nanofluid is given by [51],

$$k_{nf} = \frac{(k_s + 2k_{bf}) + 2\phi(k_s - k_{bf})}{(k_s + 2k_{bf}) - \phi(k_s - k_{bf})} \quad (11)$$

Here, k_s is thermal conductivity of solid nanoparticle, k_{bf} is thermal conductivity of base fluid and k_{nf} is thermal conductivity of nanofluid. Equation (11) doesn't take into account the nanoparticle size, which is actually a very influential factor. However, the effect is minimal for nanoparticle diameter greater than 30 nm [52]. As a result, this equation was used in this study for its simplicity. Three different nanofluids have been studied, Al₂O₃-water, CuO-water and TiO₂-water.

As numerical analysis of an approximation of real-life experimental conditions, there is bound to be some sort of deviation of the predicted value from experimental value. The amount of deviation is measured by error, which is the ratio of the difference between experimental and simulated result to the experimental result. In this study, absolute value of the relative errors have been used in all cases, which is given by,

$$\epsilon = \left| \frac{V_{exp} - V_{sim}}{V_{exp}} \right| \times 100\% \quad (12)$$

Here, V indicates the value of the corresponding parameter. This equation is applicable for both f and Nu .

In this study, it was assumed that water is incompressible and its properties such as density, viscosity, thermal conductivity, etc. are independent of temperature T . This made numerical computation much easier and quicker. The assumption of incompressibility, however, is not so straightforward for nanofluids even though the base fluid is incompressible. The thermophysical characteristics

of nanofluid flow are yet not fully explained. Thus, there have been numerical studies with the assumption of both compressibility and incompressibility for nanofluid flow. However, Buongiorno [52], in his work, described the assumption of incompressibility accurate for liquid nanofluids. This is why numerous recent studies considered nanofluid as a single-phase incompressible fluid when the base fluid is water or any other liquid [53–55]. This work, therefore, assumed nanofluids incompressible for the CFD-based studies. The properties taken for pure water and other materials used in the CFD simulations are presented in Table 2.

3.3 Computational fluid dynamics (CFD)

In this work, a CFD tool i.e. COMSOL Multiphysics was employed to predict thermal–hydraulic characteristics in rib-roughened narrow channels. The channel and the micro-ribs were assumed to be constructed with copper, and the flowing fluid was water. Heat transfer through the solid ribs is governed by the conservation of energy (Eq. (13)) and Fourier’s law (Eq. (14)). It has been assumed that the whole heat transfer process occurs under steady state condition.

$$(\nabla \cdot \dot{\mathbf{q}}) = \dot{\mathbf{E}} \tag{13}$$

$$\dot{\mathbf{q}} = -k\nabla T \tag{14}$$

Here, $\dot{\mathbf{q}}$ is heat flux vector, $\dot{\mathbf{E}}$ is heat generation vector and T is temperature. On the other hand, heat transfer in water is governed by the Navier–Stokes equations. The heat equation for an incompressible fluid medium, where the work done by pressure and viscous heating is negligible, is given by,

$$\rho C_p((\mathbf{u} \cdot \nabla)T) + (\nabla \cdot \dot{\mathbf{q}}) = \dot{\mathbf{E}} \tag{15}$$

Here, $\dot{\mathbf{q}}$ may be calculated using Eq. (14). The velocity vector \mathbf{u} may be calculated by simultaneously solving the continuity and momentum equations for incompressible flow given by,

$$\nabla \cdot \mathbf{u} = 0 \tag{16}$$

$$\rho \frac{\partial \mathbf{u}}{\partial t} + \mathbf{u} \cdot \nabla \mathbf{u} = \nabla \cdot (\mu \cdot (\nabla \mathbf{u} + (\nabla \mathbf{u})^T) - P\mathbf{I}) + \mathbf{F} \tag{17}$$

Here \mathbf{F} is body force vector, \mathbf{I} is identity matrix, t is time and P is static pressure.

3.4 κ - ϵ Turbulence model

In this study, it was assumed that flow through the rib-roughened narrow channel is turbulent, which is a logical assumption for most forced flow conditions of liquid coolant. Therefore, the κ - ϵ turbulent flow model was selected for CFD-based simulations. This turbulence model is one of the most extensively used ones and is proven to be quite accurate for internal flow of a fluid i.e. flow through a channel or pipe provided that the surface is smooth.

In κ - ϵ turbulence model, two transport equations are solved along with the Navier–Stokes equations. These two equations contain two additional dependent variables, the turbulence kinetic energy κ and the turbulence dissipation rate ϵ . The two transport equations are,

$$\rho \frac{\partial \kappa}{\partial t} + \rho \mathbf{u} \cdot \nabla \kappa = \nabla \cdot \left(\left(\mu + \frac{\mu_T}{\sigma_\kappa} \right) \nabla \kappa \right) + p_\kappa - \rho \epsilon \tag{18}$$

$$\rho \frac{\partial \epsilon}{\partial t} + \rho \mathbf{u} \cdot \nabla \epsilon = \nabla \cdot \left(\left(\mu + \frac{\mu_T}{\sigma_\epsilon} \right) \nabla \epsilon \right) + C_{\epsilon 1} \frac{\epsilon}{\kappa} p_\kappa - C_{\epsilon 2} \rho \frac{\epsilon^2}{\kappa} \tag{19}$$

Here μ_T and p_κ are turbulence viscosity and production term respectively. These two may again be calculated using Eqs. (20) and (21) respectively.

$$\mu_T = \rho C_\mu \frac{K^2}{\epsilon} \tag{20}$$

$$p_\kappa = \mu_T \left(\nabla \mathbf{u} : (\nabla \mathbf{u} + (\nabla \mathbf{u})^T) - \frac{2}{3} (\nabla \cdot \mathbf{u})^2 \right) - \frac{2}{3} \rho \kappa \nabla \cdot \mathbf{u} \tag{21}$$

In Eqs. (18–20), five adjustable model parameters C_μ , $C_{\epsilon 1}$, $C_{\epsilon 2}$, σ_κ and σ_ϵ are present. These constant parameters

Table 2 Properties of different materials considered for numerical study

	ρ (kg/m ³)	C_p (J/kg.K)	k_T (W/m.K)	μ (N.s/m ²)
Pure water	1000	4200	0.60	0.001
Al ₂ O ₃	3960 [56]	773 [56]	40 [56]	–
CuO	6000 [56]	551 [56]	33 [56]	–
TiO ₂	4230 [56]	692 [56]	8.4 [56]	–
Al ₂ O ₃ -water	1059.2 (Eq. 18)	3943.75 (Eq. 20)	0.635 (Eq. 19)	0.00113 [51]
CuO-water	1100 (Eq. 18)	3801.93 (Eq. 20)	0.635 (Eq. 19)	0.00243 [51]
TiO ₂ -water	1064.6 (Eq. 18)	3921.23 (Eq. 20)	0.63 (Eq. 19)	0.00154 [51]

may be adjusted for better performance of the turbulence model. The default values of these turbulence model parameters and their suggested ranges are presented in Table 3. The ranges of the κ - ϵ turbulence model parameters are found to vary from one study to another in the literature [35, 37, 38]. However, the ranges suggested by Guillas, Glover and Malki-Epshtein [35] are found to be sufficiently wide and thus have been adopted.

While C_μ , $C_{\epsilon 1}$, $C_{\epsilon 2}$ and σ_k are independent from each other, σ_ϵ is dependent on C_μ , $C_{\epsilon 1}$, $C_{\epsilon 2}$. The relationship is shown in Eq. (22),

$$\sigma_\epsilon = \frac{C_\kappa}{\sqrt{C_\mu}(C_{\epsilon 2} - C_{\epsilon 1})} \quad (22)$$

Here, C_κ is Von Kármán constant. Therefore, the value of σ_ϵ must be altered in such a manner that Eq. (22) holds. In this study, the four independent turbulence model parameters were calibrated so that the accuracy of κ - ϵ turbulent model improved while analyzing the thermal-hydraulic characteristics of water flowing inside rib-roughened narrow channel.

While κ - ϵ turbulent model is applicable for most portions of the fluid domain, the equations for the model are not valid near the walls. This is because the equations are derived assuming that Reynolds number is high, which is not true near the wall of the channel. The law of the walls state that the turbulence near the boundary is a function of the flow conditions of the wall only and is independent of the flow at a large distance [58]. This law is applicable for a fluid layer near the walls known as the viscous sub-layer. In this region, Eq. (23) holds.

$$u^+ = y^+ \quad (23)$$

Here, u^+ and y^+ are dimensionless velocity and dimensionless length respectively. These two parameters are obtained from Eqns. 24 and 25 respectively.

$$u^+ = \frac{\bar{u}}{u_\tau} \quad (24)$$

$$y^+ = \frac{\rho u_\tau y}{\mu} \quad (25)$$

Here, \bar{u} is mean velocity, y is distance from the wall and u_τ is friction velocity defined by Eq. 26.

$$u_\tau = \sqrt{\frac{\tau_w}{\rho}} \quad (26)$$

Here, τ_w is wall shear stress. The viscous sub-layer is located up to $y^+ < 5$. For $30 \geq y^+ \geq 5$, there is a zone where neither law of walls nor standard κ - ϵ turbulent model is applicable, known as buffer zone. For $y^+ > 30$, standard κ - ϵ turbulent model gives satisfactory results, known as the logarithmic layer [58]. The velocity profile in the logarithmic layer is given by,

$$u^+ = \frac{1}{C_\kappa} \ln(y^+) + 5.2 \quad (27)$$

Since the standard κ - ϵ turbulent model is not applicable close to the walls, automatic wall treatment is done near the walls in COMSOL Multiphysics. The wall treatment in COMSOL Multiphysics is done in such a manner that the computational domain is assumed to be located a distance y_w from the wall. y_w is computed automatically in the CFD software so that,

$$y_w^+ = \frac{\rho u_\tau y_w}{\mu} = 11.06 \quad (28)$$

This corresponds to the distance where logarithmic layer would meet viscous sub-layer if there is no buffer zone. The boundary conditions for the turbulence kinetic energy κ and the turbulence dissipation rate ϵ are,

$$\mathbf{n} \cdot \nabla \kappa = 0 \quad (29)$$

$$\epsilon = \frac{C_\mu^{3/4} \kappa^{3/2}}{C_\kappa y_w} \quad (30)$$

Here, \mathbf{n} is the unit normal vector.

3.5 Multivariate nonlinear regression analysis

In this work, focus was given on reducing the combined relative error in predicting f and Nu in CFD-based simulation with κ - ϵ turbulent model. This implies that the turbulence model was calibrated in such a manner that predicted value of neither the f nor Nu has very high deviation from experimental results. For example, instead of 1% relative error for the value of the Nu and 29% relative error for the value of the f , 15% relative error for both the Nu and f is preferred. Therefore, the improvement of the turbulence model was determined on the basis of mean-squared error (MSE) which is,

Table 3 Default values and ranges for turbulence model parameters [57]

	C_μ	$C_{\epsilon 1}$	$C_{\epsilon 2}$	σ_k	σ_ϵ
Default value	0.09	1.44	1.92	1.0	1.3
Range	0.01–0.15	1.0–1.5	1.1–2.5	0.5–2.5	–

$$\epsilon_{MSE} = \frac{1}{2} \sqrt{(\epsilon_{Nu}^2 + \epsilon_f^2)} \tag{31}$$

Here, ϵ_{Nu} is relative error to predicting the Nu and ϵ_f is relative error to predicting the f . In this study, the values of the turbulence model parameters C_{μ} , $C_{\epsilon 1}$, $C_{\epsilon 2}$ and σ_k were varied in a random manner within the range specified in Table 3 and the f and Nu were calculated from the CFD simulation results. After that, they were compared with the experimental results to obtain ϵ_f and ϵ_{Nu} for each set of values of the turbulence model parameters. These data were again utilized to derive correlations between the relative errors and the turbulence model parameters using multivariate nonlinear regression analysis. Since there were four different geometric configurations for the rib-roughened narrow channels, total eight correlations were derived; four for ϵ_f and four are for ϵ_{Nu} .

For regression analysis, sample data were generated for different combinations of the turbulence model parameters. Total 75 combinations were used for data generation purpose. Figure 7 shows the distribution of the values of the model parameters taken for the regression analysis. These combinations were selected randomly considering the following restrictions:

- The values of C_{μ} , $C_{\epsilon 1}$, $C_{\epsilon 2}$ and σ_k were randomly selected within the ranges specified in Table 3. It was assumed that the values of these four turbulence parameters have uniform distribution within their respective ranges.
- Since the value of σ_{ϵ} is always positive, $C_{\epsilon 2}$ must always be greater than $C_{\epsilon 1}$. To ensure this with ease, it was assumed that there is a linear correlation between $C_{\epsilon 1}$ and $C_{\epsilon 2}$ for most of the combinations (70 out of 75). The correlation was derived in such a manner that the lowest values of $C_{\epsilon 1}$ and $C_{\epsilon 2}$ (1.0 and 1.1 respectively) were placed in one combination while the highest values (1.5 and 2.5 respectively) were in another combination. For the remaining 5 combinations, $C_{\epsilon 1}$ and $C_{\epsilon 2}$ were assumed to be fully independent of each other. This was done to include some of the combinations suggested in available literature, including the default combination of turbulence model parameters in Table 3 [57]. Although it may seem like the biased correlation between $C_{\epsilon 1}$ and $C_{\epsilon 2}$ should severely affect the effectiveness of the regression analysis, it was not the case. Even with this simplification, the regression analysis was observed to be quite efficient, as shown later on in the "Results and Discussion" section.

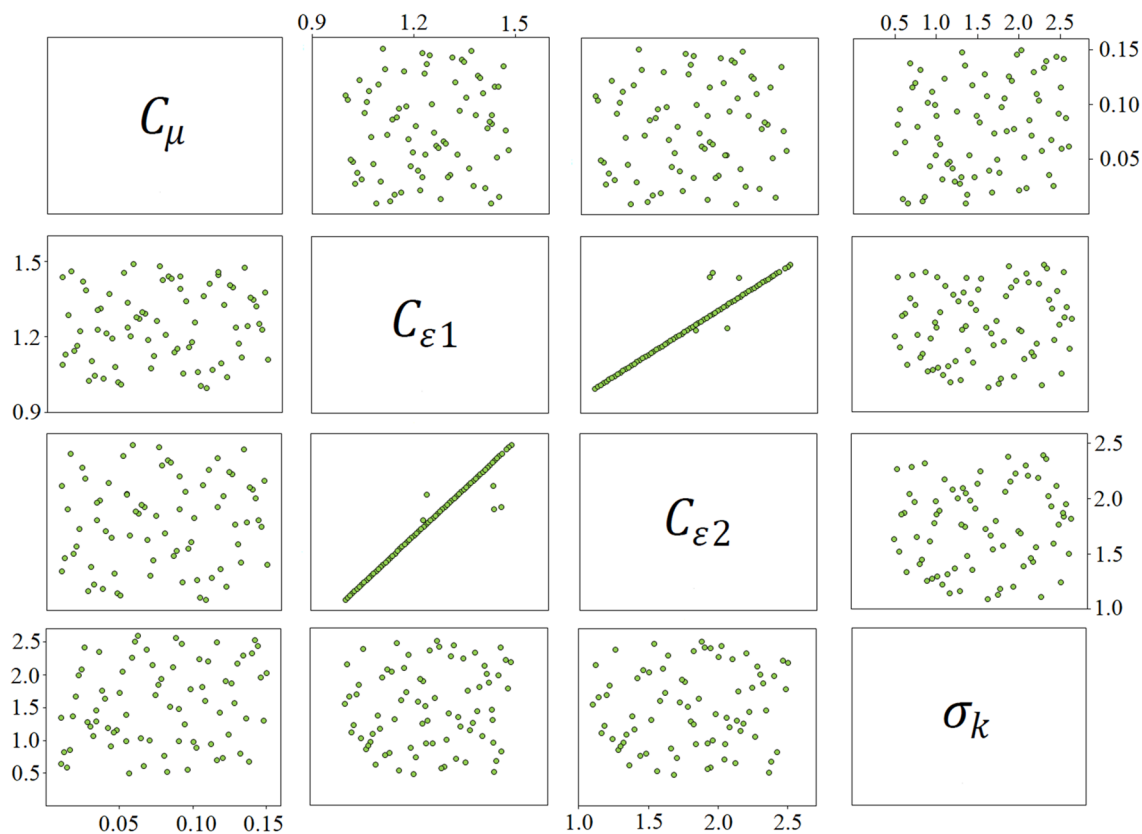


Fig. 7 Distribution of the turbulence model parameters for regression analysis

In this study, it was assumed that there exists a non-linear relationship between error and turbulence model parameters. Thus a polynomial correlation was assumed of the form presented in Eq. (32),

$$\epsilon_r = a C_\mu^{b_1} C_{\epsilon_1}^{b_2} C_{\epsilon_2}^{b_3} \sigma_k^{b_4} (C_{\epsilon_2} - C_{\epsilon_1})^{b_5} \tag{32}$$

Here, ϵ_r is relative error predicted by the correlation and $a, b_1, b_2, b_3, b_4,$ and b_5 are regression constants. The term $(C_{\epsilon_2} - C_{\epsilon_1})$ has been included in order to account for the effect of $\sigma\epsilon$ which is strongly dependent on the term. Taking logarithm of base e on both sides, we obtain,

$$\ln(\epsilon_r) = \ln(a) + b_1 \cdot \ln(C_\mu) + b_2 \cdot \ln(C_{\epsilon_1}) + b_3 \cdot \ln(C_{\epsilon_2}) + b_4 \cdot \ln(\sigma_k) + b_5 \cdot \ln(C_{\epsilon_2} - C_{\epsilon_1}) \tag{33}$$

This equation may be re-written as,

$$Y_r = A + b_1 X_1 + b_2 X_2 + b_3 X_3 + b_4 X_4 + b_5 X_5 \tag{34}$$

where,

$$Y = \ln(\epsilon); A = \ln(a); X_1 = \ln(C_\mu); X_2 = \ln(C_{\epsilon_1}) \tag{35}$$

$$X_3 = \ln(C_{\epsilon_2}); X_4 = \ln(\sigma_k); X_5 = \ln(C_{\epsilon_2} - C_{\epsilon_1}) \tag{36}$$

Now, for best fitted curve, the following equations must hold,

$$\frac{\partial S}{\partial A} = \frac{\partial S}{\partial b_1} = \frac{\partial S}{\partial b_2} = \frac{\partial S}{\partial b_3} = \frac{\partial S}{\partial b_4} = \frac{\partial S}{\partial b_5} = 0 \tag{37}$$

Here, S is the sum of squared errors presented in Eq. (38).

$$S = \sum_1^n (Y_{sim} - Y_r)^2 = \sum [\ln(\epsilon_{sim}) - \ln(\epsilon_r)]^2 \tag{38}$$

Here, ϵ_{sim} is relative error obtained from simulation results and n is the number of observations, which is equal to 75 in this study. Solving Eqs. (37), we obtain,

$$\begin{bmatrix} A \\ b_1 \\ b_2 \\ b_3 \\ b_4 \\ b_5 \end{bmatrix} = \begin{bmatrix} n & \sum X_1 & \sum X_2 & \sum X_3 & \sum X_4 & \sum X_5 \\ \sum X_1 & \sum X_1^2 & \sum X_1 X_2 & \sum X_1 X_3 & \sum X_1 X_4 & \sum X_1 X_5 \\ \sum X_2 & \sum X_1 X_2 & \sum X_2^2 & \sum X_2 X_3 & \sum X_2 X_4 & \sum X_2 X_5 \\ \sum X_3 & \sum X_1 X_3 & \sum X_2 X_3 & \sum X_3^2 & \sum X_3 X_4 & \sum X_3 X_5 \\ \sum X_4 & \sum X_1 X_4 & \sum X_2 X_4 & \sum X_3 X_4 & \sum X_4^2 & \sum X_4 X_5 \\ \sum X_5 & \sum X_1 X_5 & \sum X_2 X_5 & \sum X_3 X_5 & \sum X_4 X_5 & \sum X_5^2 \end{bmatrix} \begin{bmatrix} \sum Y_{sim} \\ \sum X_1 Y_{sim} \\ \sum X_2 Y_{sim} \\ \sum X_3 Y_{sim} \\ \sum X_4 Y_{sim} \\ \sum X_5 Y_{sim} \end{bmatrix} \tag{39}$$

These equations in matrix form may easily be solved using MATLAB to obtain the values of the regression constants. After deriving the correlations, it is necessary to identify whether the curves are good-fit or not. For this purpose, R^2 -values for each derived correlation were calculated using Eq. (39).

$$R^2 = 1 - \frac{\sum (\epsilon_{sim} - \epsilon_r)^2}{\sum (\epsilon_{sim} - \bar{\epsilon})^2} \tag{40}$$

Here, $\bar{\epsilon}$ is average of the actual error values. A R^2 -value above 0.5 represents a moderate-fit while a value greater than 0.7 represents good-fit. The correlations derived were used to construct the objective functions to be used in genetic algorithm based optimization process.

3.6 Genetic algorithm (GA) for multi-objective optimization

The GA is a nature-inspired optimization algorithm that mimics the process of natural selection to find the optimum results [40]. The core idea of natural selection is that the fittest individuals from a group of people or population survive with the passage of each generation. These individuals pass their genes to their offspring who inherit the characteristics of their parents. The fittest individuals among them again survive and pass their genes to their offspring, and the cycle keeps on going. The GA is also developed from the same idea. There are five phases considered in the genetic algorithm: initial population, fitness evaluation, selection, crossover, and mutation.

At first, a set of input parameters are randomly taken who represent the individuals of a population. The number of individuals in the population is called population size. Every individual of this population is a potential solution of the optimization problem. The set of parameters that represent the individual is call chromosome and every parameter is called gene. Each individual is characterized by a fitness value that indicates how fit the individual is. The fitness value is calculated using a fitness function which is derived to represent one or multiple objective functions

of the problem. The objective functions are the functions that are to be optimized i.e. maximized or minimized depending on the situation. On the basis of the fitness values, the individuals are selected who pass their genes to the next generation. Any two individuals from them have a probability of producing offspring. The two individuals who reproduce are called parents. The selection of parents

is also done based on their fitness values. The individual having better fitness value (either higher or lower value depending on the problem) have greater chance of taking part in reproduction process.

As two individuals mate, there is a probability of crossover of their genes in the chromosomes of the children. The crossover rate is the number of times a crossover may occur in a generation. The value of crossover rate varies in the range of 0–1. The higher the crossover rate, the lower the probability of offspring having identical chromosomes like the parents. Another important phase of the algorithm is mutation. In this phase, some of the individuals undergo random change in one or more genes of their chromosomes. This happens in a very low probability but is very essential for preventing premature termination of the iteration process. The ratio of individuals experiencing mutation to the number of individuals in a generation is called mutation rate.

These five phases occur in a cyclic order from generation to generation. Once the individuals of the new generation stop improving from the individuals of the previous generation, the iteration process stops. The individual or the set of parameters having the best fitness value is the optimum set of values. The whole iteration process in GA is shown in Fig. 8.

In this work, GA was employed in finding the best combination of turbulence model parameters for optimizing

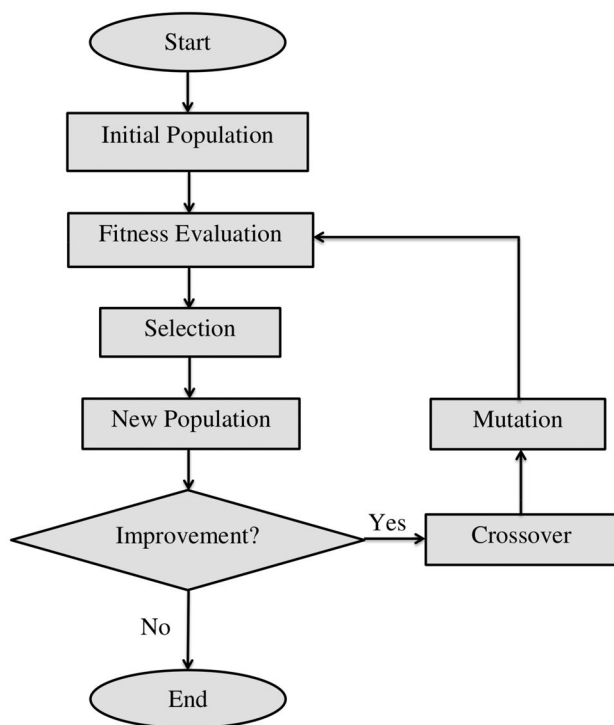


Fig. 8 Flowchart of GA

the relative errors ϵ_f and ϵ_{Nu} simultaneously for a specific configuration of the rib-roughened narrow channel. Thus, there were two objective functions in this genetic algorithm-based calibration process, ϵ_f and ϵ_{Nu} , which were introduced in Sect. 3.5 of this paper. These two objective functions are dependent on the four turbulence model parameters. The correlations for calculating the values of these objective functions are derived using the methodology presented in Sect. 3.5.

Since there were two objective functions for each narrow channel configuration, the considered problem is a multi-objective optimization. To simplify the problem, a mono-objective approach has been adopted by combining the two objective functions into a single one. In other words, a single fitness function had to be derived that represented both the objective functions. The fitness function considered in this study is given by,

$$F_v = \sqrt[4]{2 \epsilon_{MSE}} = \sqrt[8]{(\epsilon_{Nu}^2 + \epsilon_f^2)} \tag{41}$$

Since this was a minimization problem, the smaller fitness value was considered the better one. The chromosomes of each individual consisted of four genes which contained the values of the four turbulence model parameters C_μ , $C_{\epsilon 1}$, $C_{\epsilon 2}$ and σ_k as shown in Fig. 9. These values were randomly selected within their respective ranges specified in Table 3. During random sampling of the genes i.e. the turbulence model parameters, the following constraints were considered:

- $0.01 \leq C_\mu \leq 0.15$
- $1 \leq C_{\epsilon 1} \leq 1.5$
- $1.1 \leq C_{\epsilon 2} \leq 2.5$
- $0.5 \leq \sigma_k \leq 2.5$
- $(C_{\epsilon 2} - C_{\epsilon 1}) \geq 0.1$, to avoid extremely high value of σ_ϵ

For the GA-based simulations, total 10,000 individuals were taken in the initial population. The total number of individuals was kept constant for all generations. Three crossover rates were investigated 0.50, 0.70 and 0.90 while three mutation rates were considered in this study; 0.01,

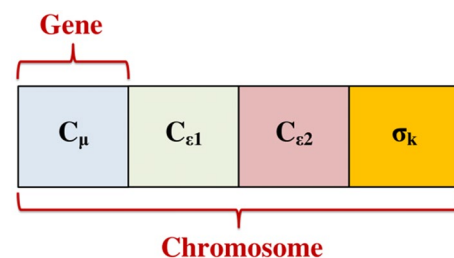


Fig. 9 Chromosome structure for the study

0.05 and 0.10 to observe influence of these two parameters on the simulation results. The iteration process was terminated if there was no improvement in the best fitness value for 100 consecutive generations. The individual with the lowest fitness value at the end of the iteration process represented the set of turbulence model parameters with optimized results in κ - ϵ turbulent model and thus was the calibrated set of turbulence model parameters. Separate MATLAB codes were developed to run the GA-based simulations for each narrow channel configuration.

4 Results and discussion

4.1 Random data generated from CFD simulations

In order to derive the correlations for ϵ_f and ϵ_{Nu} with the four κ - ϵ turbulent model parameters i.e. C_{μ} , $C_{\epsilon 1}$, $C_{\epsilon 2}$ and σ_k , data were generated with the help of COMSOL

Multiphysics, a commercially available CFD tool. 75 combinations of the turbulence model parameters were used in the data generation stage (see Sect. 3.5 for details) and both ϵ_f and ϵ_{Nu} were computed for each combination. Figures 10 and 11 show the relative errors for the f and Nu respectively for each turbulence model parameter. From Fig. 10, it may be observed that all the relative error data for f were very scattered for all four of the turbulence model parameters. No visible trend for the data could be identified. The data were the most scattered for σ_k indicating that it might have the weakest relationship with the predictive accuracy amongst the four turbulence model parameters.

From Fig. 11, it may be observed that the error data for Nu were very scattered for C_{μ} and σ_k . Thus, it is most likely that these two turbulence model parameters have a very weak relationship with ϵ_{Nu} . On the other hand, ϵ_{Nu} has decreased almost exponentially with the increase in the values of $C_{\epsilon 1}$ and $C_{\epsilon 2}$. However, it is noteworthy that

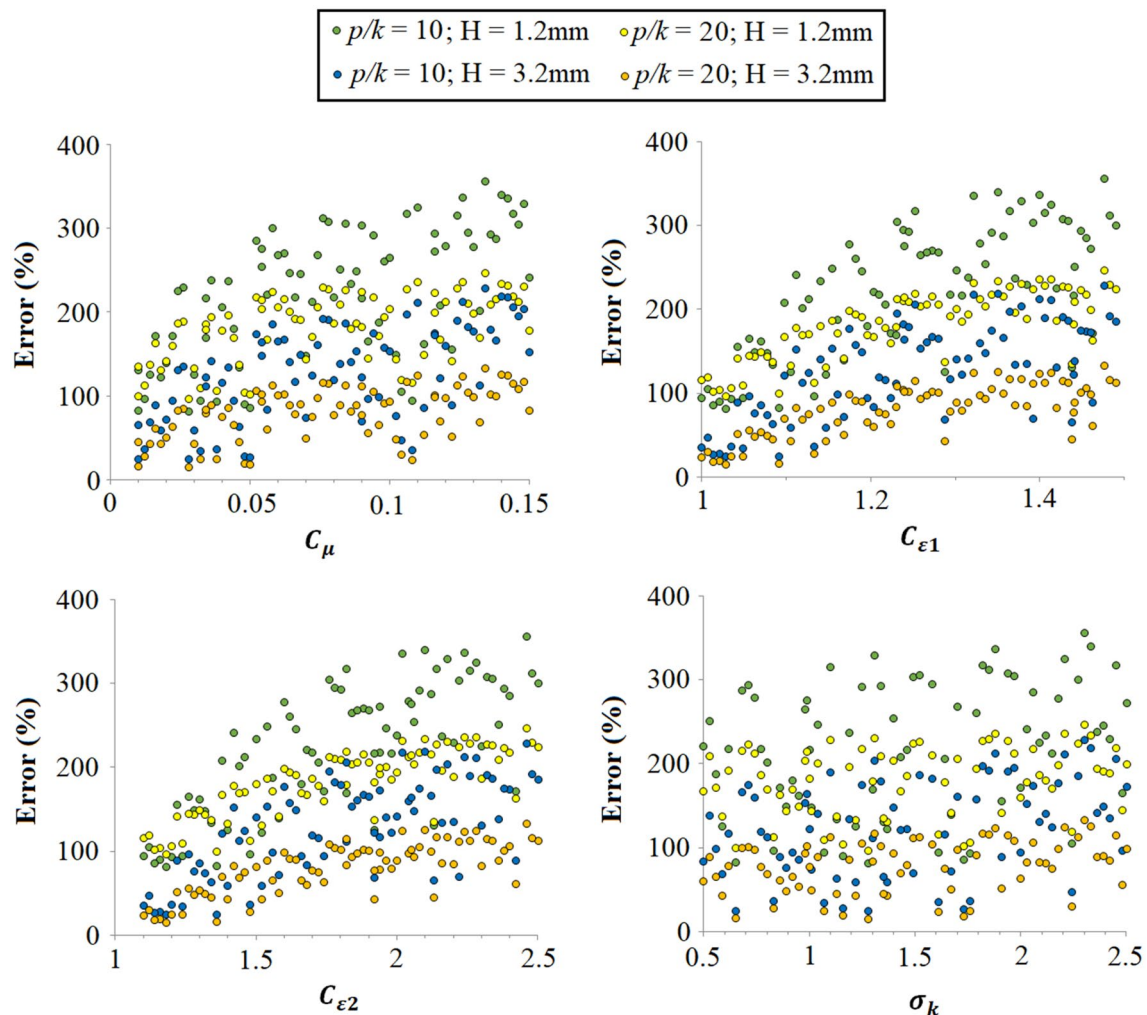


Fig. 10 Absolute values of relative errors in predicting the friction factor with κ - ϵ turbulent model

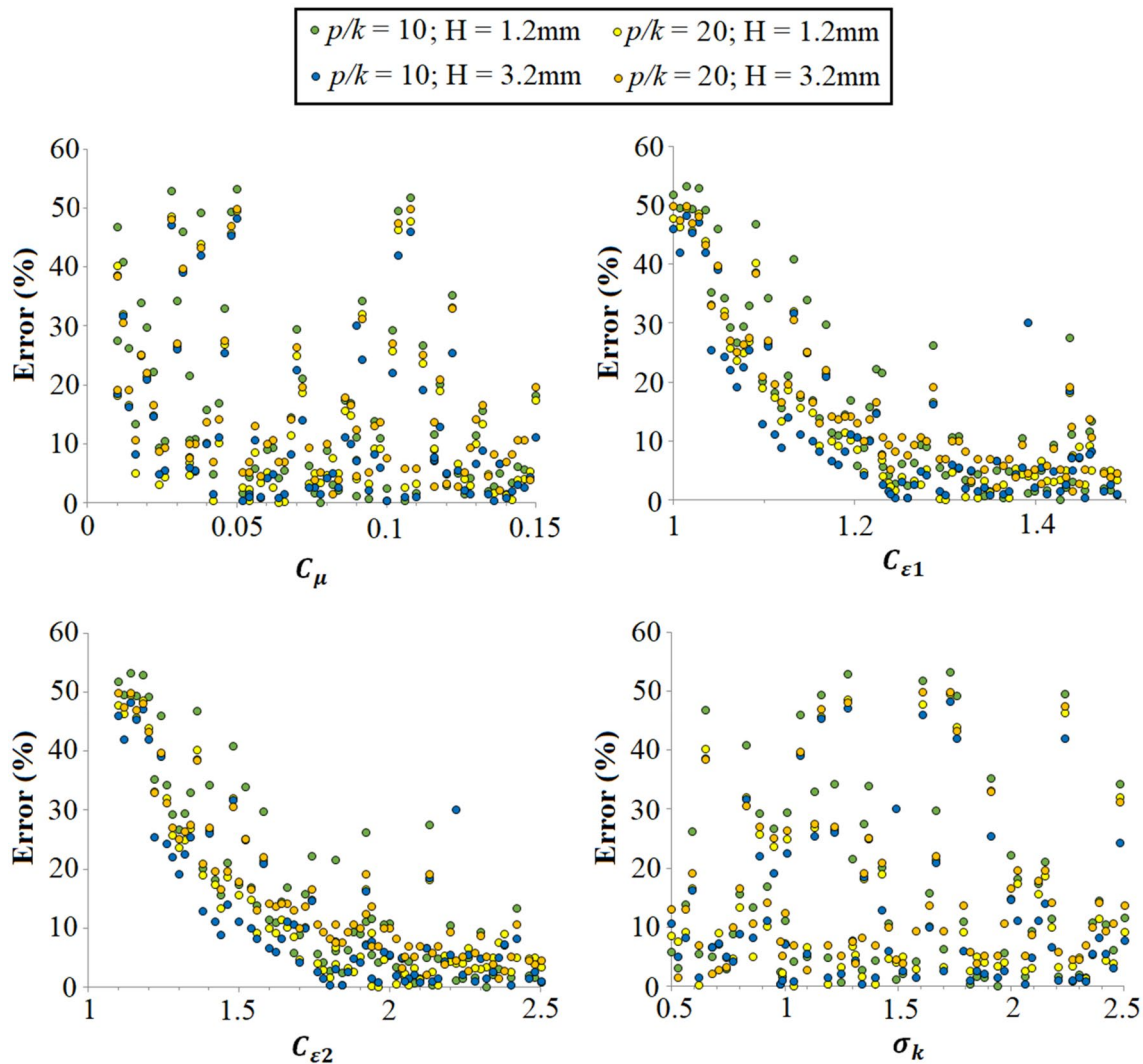


Fig. 11 Absolute values of relative errors in predicting the Nusselt number with κ - ϵ turbulent model

the values of other two model parameters are not to be neglected. Thus, Fig. 11 does not necessarily imply that both $C_{\epsilon 1}$ and $C_{\epsilon 2}$ have an inverse relationship with relative error. The effect of one may dominate the other. Nevertheless, it may be assumed that $C_{\epsilon 1}$ and $C_{\epsilon 2}$ are possibly the key parameters for the calibration process. Another finding from Fig. 11 is that the correlations of ϵ_{Nu} with the four turbulence model parameters are certainly nonlinear, making the assumption considered in Sect. 3.5 valid. An important observation from Figs. 10 and 11 is that the values of ϵ_f were, for most cases, much higher than the ones of ϵ_{Nu} .

4.2 Correlations derived from multivariate nonlinear regression analysis

Using the data presented in Figs. 10 and 11, correlations were developed for each narrow channel configuration

using Multivariate Nonlinear Regression Analysis presented in Sect. 3.5. The derived correlations are presented in Table 4. From Table 4, it may be observed that for all the correlations, R^2 -values are above 0.5, making all of them either moderate or good-fits. The R^2 -values are comparatively higher for correlations of ϵ_{Nu} than that of ϵ_f . Also, for channel height of 1.2 mm, the derived correlations have a better R^2 -value compared to the channel height of 3.2 mm. Therefore, it may be assumed that the calibration process using GA simulation should be more effective for $H = 1.2$ mm than for $H = 3.2$ mm.

From Table 4, it may also be observed that the relative errors of both the f and Nu are, indeed, weakly affected by the values of $C_{\mu'}$ ($C_{\epsilon 1}$ - $C_{\epsilon 2}$) and σ_k , which was predicted earlier in this section. They, however, are highly related to $C_{\epsilon 1}$ and $C_{\epsilon 2}$. Therefore, it is evident that calibrating these two values are of prime importance in this study. Another

Table 4 Derived correlations using multivariate nonlinear regression method

Channel configuration	Parameter	Derived correlation	R ² -Value
$p/k=10$; $H=1.2$ mm	f	$f_f = 82.922C_{\mu}^{0.0014}C_{\epsilon_1}^{-2.3660}C_{\epsilon_2}^{2.4489}\sigma_k^{0.2256}(C_{\epsilon_2} - C_{\epsilon_1})^{0.0278}$	0.62
	Nu	$f_{Nu} = 186.7741C_{\mu}^{0.0026}C_{\epsilon_1}^{8.4383}C_{\epsilon_2}^{-8.5916}\sigma_k^{-0.3097}(C_{\epsilon_2} - C_{\epsilon_1})^{-0.0614}$	0.70
$p/k=20$; $H=1.2$ mm	f	$f_f = 98.0032C_{\mu}^{0.0007}C_{\epsilon_1}^{-1.5322}C_{\epsilon_2}^{1.5894}\sigma_k^{0.1121}(C_{\epsilon_2} - C_{\epsilon_1})^{0.0152}$	0.72
	Nu	$f_{Nu} = 123.5938C_{\mu}^{-0.0023}C_{\epsilon_1}^{11.0414}C_{\epsilon_2}^{-9.4150}\sigma_k^{-0.0018}(C_{\epsilon_2} - C_{\epsilon_1})^{-0.0362}$	0.82
$p/k=10$; $H=3.2$ mm	f	$f_f = 30.8736C_{\mu}^{0.0026}C_{\epsilon_1}^{-3.4958}C_{\epsilon_2}^{3.4572}\sigma_k^{0.3765}(C_{\epsilon_2} - C_{\epsilon_1})^{0.0369}$	0.55
	Nu	$f_{Nu} = 133.1931C_{\mu}^{-0.0015}C_{\epsilon_1}^{11.8412}C_{\epsilon_2}^{-9.8098}\sigma_k^{-0.3866}(C_{\epsilon_2} - C_{\epsilon_1})^{-0.0532}$	0.76
$p/k=20$; $H=3.2$ mm	f	$f_f = 26.5253C_{\mu}^{0.0022}C_{\epsilon_1}^{-3.0951}C_{\epsilon_2}^{2.9457}\sigma_k^{0.3070}(C_{\epsilon_2} - C_{\epsilon_1})^{0.1468}$	0.65
	Nu	$f_{Nu} = 83.4544C_{\mu}^{0.0007}C_{\epsilon_1}^{4.7565}C_{\epsilon_2}^{-5.5103}\sigma_k^{0.2081}(C_{\epsilon_2} - C_{\epsilon_1})^{-0.0352}$	0.88

important observation is that ϵ_f increases with decreasing value of C_{ϵ_1} and increasing value of C_{ϵ_2} . On the other hand, ϵ_{Nu} increases with an increasing value of C_{ϵ_1} and a decreasing value of C_{ϵ_2} . Thus, it may be understood that decreasing ϵ_f will essentially increase ϵ_{Nu} and vice versa.

4.3 Calibration values of the turbulence model parameters

After obtaining the required correlations, they were used as the objective functions in the GA-based simulations. Separate MATLAB codes were developed for each narrow channel configuration. The fitness values were calculated using Eq. 41. Figure 12 shows the plots of the best fitness values and average fitness values with the progression of each generation in the simulation domain for some of the trial runs of the GA-codes. From Fig. 12, it may be observed that for $H=1.2$ mm, the best fitness values at the end of the simulation process were 3.294 and 3.272 for $p/k=10$ and $p/k=20$ respectively. On the other hand, for $H=3.2$ mm, the best fitness values were 2.684 and 2.431 for $p/k=10$ and $p/k=20$ respectively. Thus, it may be stated that the minimum achievable MSEs for $H=1.2$ mm is higher than the ones for $H=3.2$ mm.

The GA-based simulations were run 10 times for each narrow channel configuration. In order to observe whether crossover and mutation rates have any influence on the final results of the GA-based simulations, multiple combinations of crossover and mutation rates were investigated for $p/k=10$, $H=3.2$ mm narrow channel configurations. Three crossover rates, 0.50, 0.70 and 0.90, were taken with a fixed mutation rate 0.05. On the other hand, three mutation rates, 0.01, 0.05 and 0.10, were taken with a fixed crossover rate 0.50. The simulation results for different combinations of crossover and mutation rates are presented in Table A-1 and A-2 in the Appendix. The mean calibration values are presented in Table 5. From Table 5, it may be observed that the mean calibration values were unaffected by the crossover and mutation rates. This may be due to the large initial population (10,000) used during

the GA-based simulations that have minimized the influence of crossover and mutation rates. For a smaller population size, 10–100 for example, this might not have been the case.

After confirming that the influence of crossover and mutation rates is insignificant, GA-based simulations for the other narrow channel configurations were conducted for crossover rate 0.50 and mutation rate 0.05 only. The simulation results are presented in Table A-3 in the Appendix. Table 6 presents the mean values of the GA-based simulations for all the narrow channel configurations. Table 6 also presents a comparison between the predicted and actual fitness values for the prospective calibrated turbulence model parameters suggested by GA-based simulations. The actual fitness values are obtained by running CFD-based simulations again with the calibrated values of turbulence model parameters. Also, some of the combinations of turbulence model parameters showed exceptionally superior performances of the κ - ϵ turbulent model during the random data generation stage of the CFD-based simulations. The combinations from the random simulation data with the best i.e. lowest fitness values have also been recorded in Table 6. This has been done due to the fact that GA-based simulations were run on the basis of correlations from a regression analysis. These correlations are approximate in nature. As a result, the calibrated values of turbulence model parameter suggested by GA-based simulations may or may not actually be the best performing ones. Thus, the final calibration was done in such a manner that: (i) if the actual fitness value for the combination of turbulence model parameters obtained from GA-based simulation is lower than that for the combination of parameters with minimum fitness value obtained during a random data generation stage, the former is accepted as the final calibrated turbulence model parameters, (ii) if the opposite case is true, the latter one is accepted as the final calibrated turbulence model parameters.

From Table 6, it may be observed that for $H=1.2$ mm, the calibrated values of turbulence model parameters suggested by GA-based simulations have superior fitness

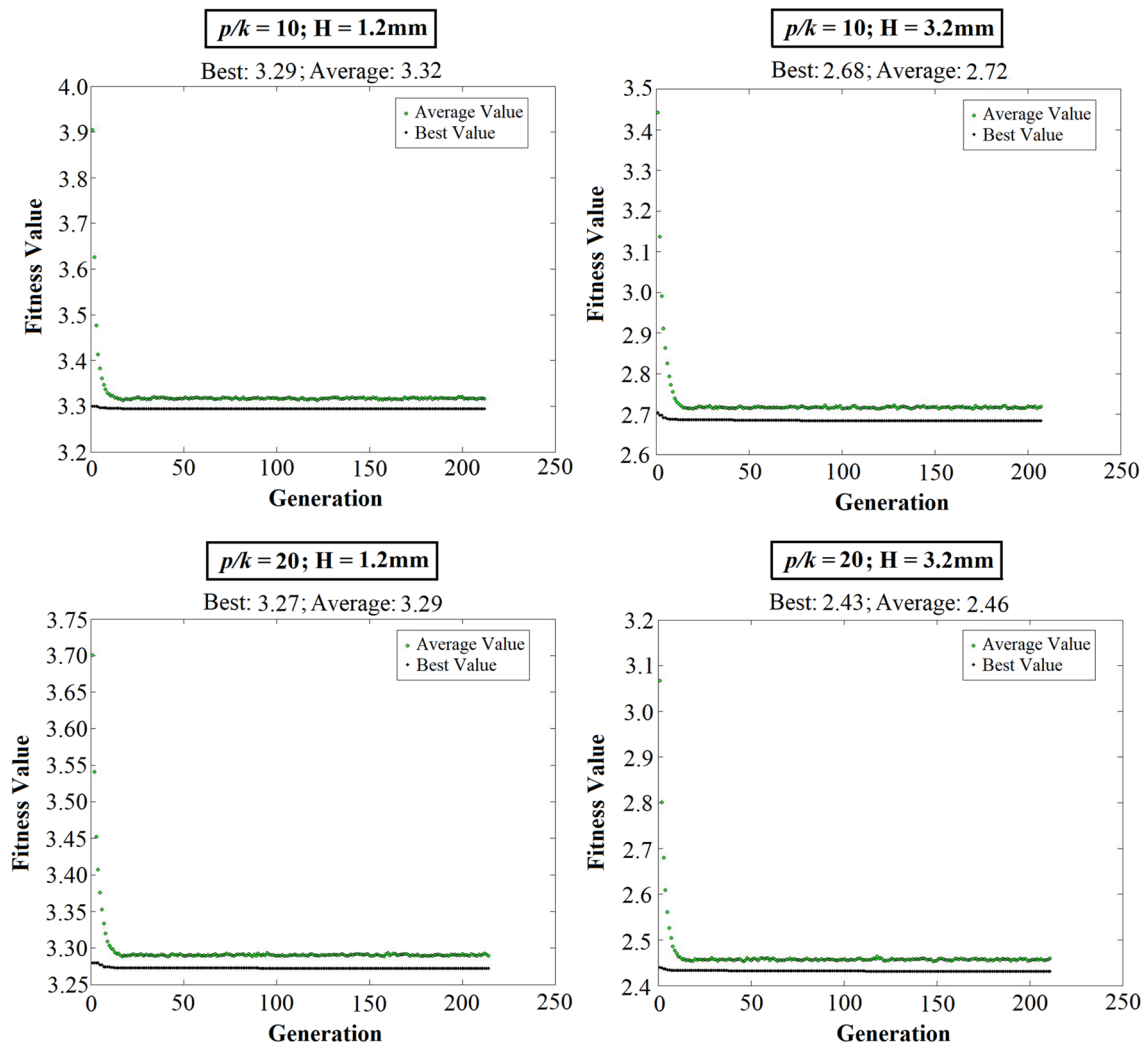


Fig. 12 Fitness value plot from genetic algorithm-based simulations for crossover rate 0.5 and mutation rate 0.05

Table 5 Mean calibration values obtained from GA-based simulations for different crossover and mutation rates and $p/k=10$, $H=1.2$ mm narrow channel configuration

Crossover rate	Mutation rate	C_{μ}	$C_{\epsilon 1}$	$C_{\epsilon 2}$	σ_k
0.50	0.01	0.01	1.00	1.20	0.50
	0.05	0.01	1.00	1.20	0.50
	0.10	0.01	1.00	1.20	0.50
0.70	0.05	0.01	1.00	1.20	0.50
0.90	0.05	0.01	1.00	1.20	0.50

values over the values obtained from a random data generation stage. Thus, the values suggested by GA-based simulations were taken as the final calibrated values. On the other hand, for $H=3.2$ mm, the values obtained a from

random data generation stage have superior fitness values over the suggested values of GA-based simulations. The possible explanation for this observation is that R^2 -values of the correlations for ϵ_f were lower for $H=3.2$ mm (0.55 and 0.65 for $p/k=10$ and $p/k=20$ respectively) than the values for $H=1.2$ mm (0.62 and 0.72 for $p/k=10$ and $p/k=20$ respectively) for the same pitch-to-height ratio, as seen from Table 4. In other words, the correlations for ϵ_f used in the GA-based simulations were more reliable for $H=1.2$ mm than $H=3.2$ mm. As a results, the GA-based simulation process was able to predict fitness values more accurately for $H=1.2$ mm than $H=3.2$ mm, which may easily be observed from Table 6. Thus, for $H=3.2$ mm, the combination of values of turbulence model parameters obtained during random data generation stage was taken as the final calibrated values.

Table 6 Comparison between predicted and actual fitness values for prospective calibration values

Channel configuration	C_μ	$C_{\epsilon 1}$	$C_{\epsilon 2}$	σ_k	Predicted ϵ_{Nu}	Actual ϵ_{Nu}	Predicted ϵ_f	Actual ϵ_f	Predicted fitness value	Actual fitness value
$p/k=10$; H=1.2 mm	Data	0.01	1.09	1.36	0.65	–	–	–	–	3.12
	GA	0.01	1.00	1.20	0.50	55.96	46.89	103.62	80.69	3.29
$p/k=10$; H=3.2 mm	Data	0.01	1.09	1.36	0.65	–	–	–	–	2.60
	GA	0.02	1.00	1.22	0.50	26.90	38.57	44.36	24.47	2.68
$p/k=20$; H=1.2 mm	Data	0.01	1.09	1.36	0.65	–	–	–	–	3.22
	GA	0.02	1.00	1.13	0.50	44.46	40.21	105.67	90.29	3.27
$p/k=20$; H=3.2 mm	Data	0.01	1.13	1.48	0.83	–	–	–	–	2.53
	GA	0.02	1.50	1.77	0.50	22.09	30.58	27.09	7.66	2.43

4.4 Model validation after calibration

It is noteworthy that the calibrated values were obtained for a fixed flow condition, $v=5$ m/s and also for scaled-down geometry. It is necessary to identify whether the geometry and Re have any effect on the performance of the calibrated turbulence model or not. To do so, a validation study was conducted. CFD-based simulations were run again for both default and calibrated values of turbulence model parameters in full-scale i.e. 200 mm heated length and 50 mm insulated length. The velocities of flow were varied in the range 1-15 m/s. Figures 13 and 14 present the values of f and Nu obtained from experimental correlations [3, 47, 53] and CFD-based simulations for 1.2 mm and 3.2 mm height of smooth and rib-roughened narrow channels respectively. For smooth channel flow, recalibration process was not conducted since the existing

κ - ϵ turbulent model itself is calibrated for smooth channels. From Figs. 13 and 14, it may be observed that the calibration process increased the accuracy in predicting the values of f with CFD employing κ - ϵ turbulent model with the expense of accuracy in predicting the value of Nu . From Fig. 13, it may be observed that the accuracy of the calibrated turbulence model in predicting both f and Nu increased with the increase in Re when $H=1.2$ mm. On the other hand, from Fig. 14, it may be observed that the accuracy in predicting Nu with the calibrated model increased with increasing Re when $H=3.2$ mm. However, from Fig. 14, it may be observed that the predicted value of f converged with the experimental value at a certain Re and then started diverging from there. Another interesting observation is that for $H=3.2$ mm, the rate of increase in accuracy in predicting Nu with the increase in Re was

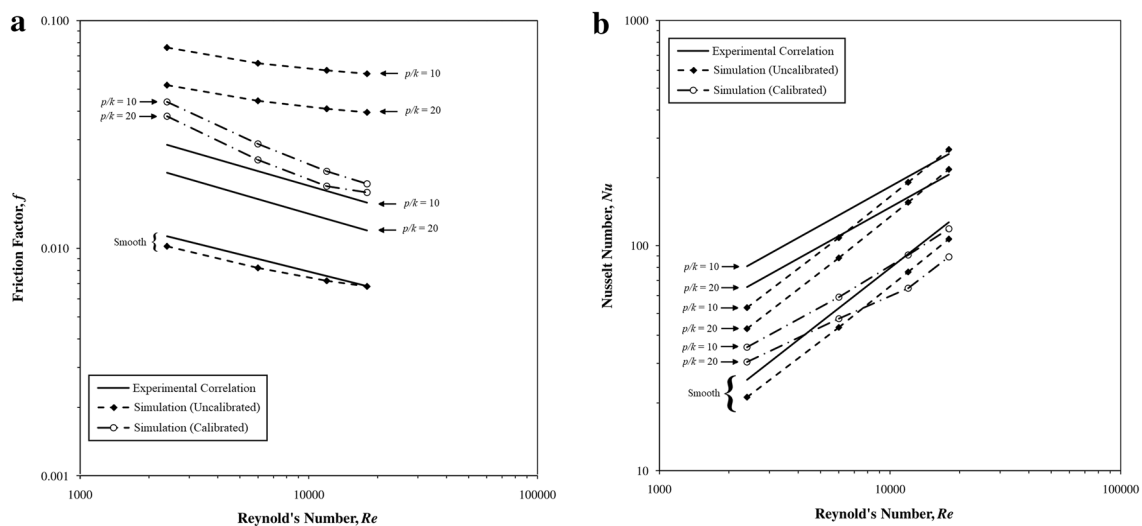


Fig. 13 Comparison of simulated friction factors with experimental correlations for channel height, $H=1.2$ mm, **b** Comparison of simulated Nusselt numbers with experimental correlations for channel height, $H=1.2$ mm

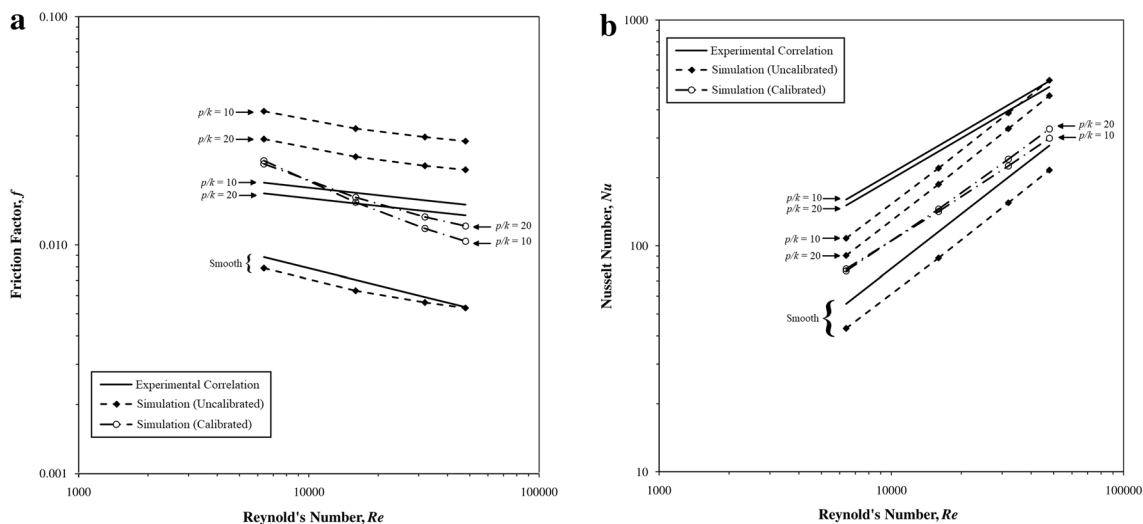


Fig. 14 Comparison of simulated friction factors with experimental correlations for channel height, $H=3.2$ mm, **b** Comparison of simulated Nusselt numbers with experimental correlations for channel height, $H=3.2$ mm

greater for $p/k=20$ than $p/k=10$. There was a similar observation for f .

Another important observation from Figs.13 and 14 is that the standard $\kappa-\epsilon$ turbulent model has good accuracy in predicting the f for smooth channels but there is a noticeable deviation of the simulated values of Nu from the experimental correlations. This is why the simulated Nu for both calibrated and uncalibrated turbulence models are observed to be lower than the experimental values for most cases of Re . The simulated results suggest that up to 1.67 and 1.43 times higher values of Nu can be obtained for $H=1.2$ mm and $p/k=10$ and 20 respectively. Also, up to 1.83 and 1.79 times higher values of Nu can be obtained for $H=3.2$ mm and $p/k=10$ and 20 respectively. The only limitation observed for the calibrated $\kappa-\epsilon$ turbulent model for $p/k=20$ mm and $H=1.2$ mm is that it predicts a lower value of Nu for the rib-roughened channel than that of a smooth channel for $Re > 7000$, which is not possible. This indicates that the effect of Re on the calibration process should not be neglected. It is also noteworthy that completely different calibrated combinations of the turbulence model parameters were used for each narrow channel configuration. This is why the curves obtained from calibrated CFD simulations are not parallel for $p/k=10$ and $p/k=20$ for the same channel height, in contrast to the curves of experimental correlations and uncalibrated CFD simulations.

From Figs.13 and 14, it is difficult to understand whether there is really an improvement of the turbulence model or not. Figure 15 represents the percent improvement or decrease in fitness value after calibration. From Fig.15, it may be observed that due to the calibration process, up to 35.83% and 27.30% improvements in the fitness values

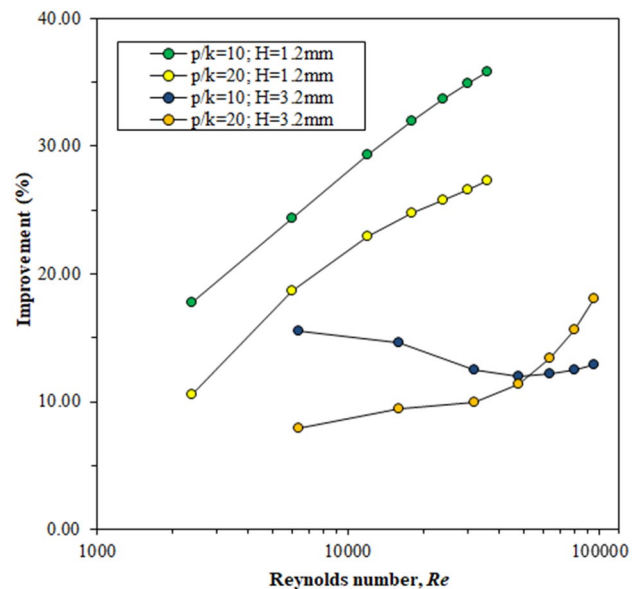


Fig. 15 Percent improvement of fitness values after calibration for different narrow channel and flow configurations

of the simulation results was obtained for $p/k=10$ and $p/k=20$ respectively when $H=1.2$ mm and $Re=35,955$. The percent improvement increased with the increase in Re . Similarly, up to 15.48% and 18.05% improvements in the fitness values were obtained for $p/k=10$ and $p/k=20$ respectively when $H=3.2$ mm. However, for $p/k=10$, improvement was greater for the lower value of Re and for $p/k=20$, improvement was greater for the higher value of Re . Nevertheless, the calibration process has significantly improved the turbulence model for all narrow channel

geometries and flow configurations. Thus, it may be stated that the improved or calibrated κ - ϵ turbulent model is superior to the default turbulence model.

It may be noted that the obtained calibration values of the turbulence model parameters are applicable only for the rectangular narrow channel geometries considered in this study i.e. $p/k=10$ and 20 and $H=1.2$ mm and 3.2 mm. From Table 6, it may be observed that the calibration values are unique for all the studied narrow channel configurations. Therefore, these calibration values may or may not be applicable for narrow channels other than the ones considered in this study. However, the calibration values should be independent on the length of the channel since they ensured better performance for both scaled-down and full-scale channel geometries. Also, the calibration values are equally applicable for constant temperature and constant heat flux boundary condition of the rib-roughened side, since Nu is independent of boundary condition of a channel for turbulent flow [47]. Finally, the calibration values should be applicable for 3D extension of the CFD study for these rib-roughened narrow channels. This is because the two other sides of the channel that were not present in the 2D models are smooth and insulated, thus should not have much contribution to either frictional head loss or convective heat transfer.

4.5 Predicted heat transfer enhancements with nanofluids

Once it was evident that the calibrated turbulence model performs better than the uncalibrated one, the calibrated turbulence model was utilized to study nanofluid flow through the same narrow channels. In this work, three nanofluids were studied, Al_2O_3 -water, CuO-water, and TiO_2 -water, each having a nanoparticle volume fraction $\phi = 0.02$ and 30 nm average nanoparticle diameter. Figure 16 shows the comparison of the predicted values of the heat transfer coefficient (h) obtained from the CFD simulations for pure water and different nanofluids using the improved turbulence model.

From Fig.16, it may be observed that CuO-water nanofluid has significantly higher predicted values of h that of pure water. The logical explanation is that CuO-water nanofluid has about twice as high Prandtl number as that of pure water, which resulted in a higher value of Nu . TiO_2 -water nanofluid is also predicted to have higher values of h than pure water. However, the values of h for TiO_2 -water nanofluid are predicted to be lower than that of CuO-water nanofluid for the same Re . Finally, Al_2O_3 -water nanofluid is predicted to have h very close to that of pure water, indicating the least performance among the three studied nanofluids. Another interesting observation is that the differences in h increase with an increase in

Re . However, from Table 7, it may be observed that the ratios of the Nusselt numbers of a specific nanofluid and pure water is found to be almost a constant for all Re . For Al_2O_3 -water nanofluid, the ratio is around 1.001 while for CuO-water nanofluid, it is around 1.32. For TiO_2 -water nanofluid, the ratio is around 1.132.

It is noteworthy that the results for nanofluids presented in Fig.16 and Table 7 should be viewed as preliminary predictions before experimental validation. To the authors' knowledge, there is no experimental or numerical simulation-based work in the available literature that dealt with nanofluids with the same narrow channel configurations. As a result, a validation study for heat transfer enhancement could not be performed in the present work. Also, the values of f for the nanofluids were found to be equal to that of pure water from the CFD simulations for the same Re . This is due to the fact that f is, theoretically, a function of Re only [3, 59], thus independent of the fluid medium as long as Re is the same. However, this may or may not be the case for nanofluids since the nanoparticles may settle down on the surface of the narrow channel and increase roughness, increasing friction factor. Therefore, further experimental studies have to be conducted to know how much the CFD results deviate from the real-life scenario.

5 Conclusion

Thermal-hydraulic characteristics in a turbulent flow regime inside a rib-roughened narrow channel for high heat flux removal still largely remain as a challenging subject that needs further study. In this numerical study, the predicting capability of κ - ϵ turbulence model is improved by calibrating four turbulence model parameters, C_{μ} , $C_{\epsilon 1}$, $C_{\epsilon 2}$ and σ_k for evaluating the f , Nu and h in a rib-roughened narrow channel with $p/k=10$ and 20 and $H=1.2$ and 3.2 mm. Square micro-ribs of 0.2 mm height are placed on the heated wall of 200 mm length while the other walls of the channel are kept smooth. Water is taken as the coolant with inlet temperature and velocity as 15 °C and 5 m/s respectively. The temperature of the heated wall is kept constant at 30 °C. Pure water and three other nanofluids, Al_2O_3 -water, CuO-water, and TiO_2 -water, have been considered for heat transfer enhancement studies. This is done by reducing the mean-squared error to predicting friction factor and Nusselt number.

In the first stage of the study, a large number of sample data have been generated using 2-dimensional CFD simulations. To reduce computation time, the heating length has been scaled down from 200 to 20 mm by keeping the entry and exit regions unchanged. Using the sample data, necessary correlations for relative errors in predicting the f

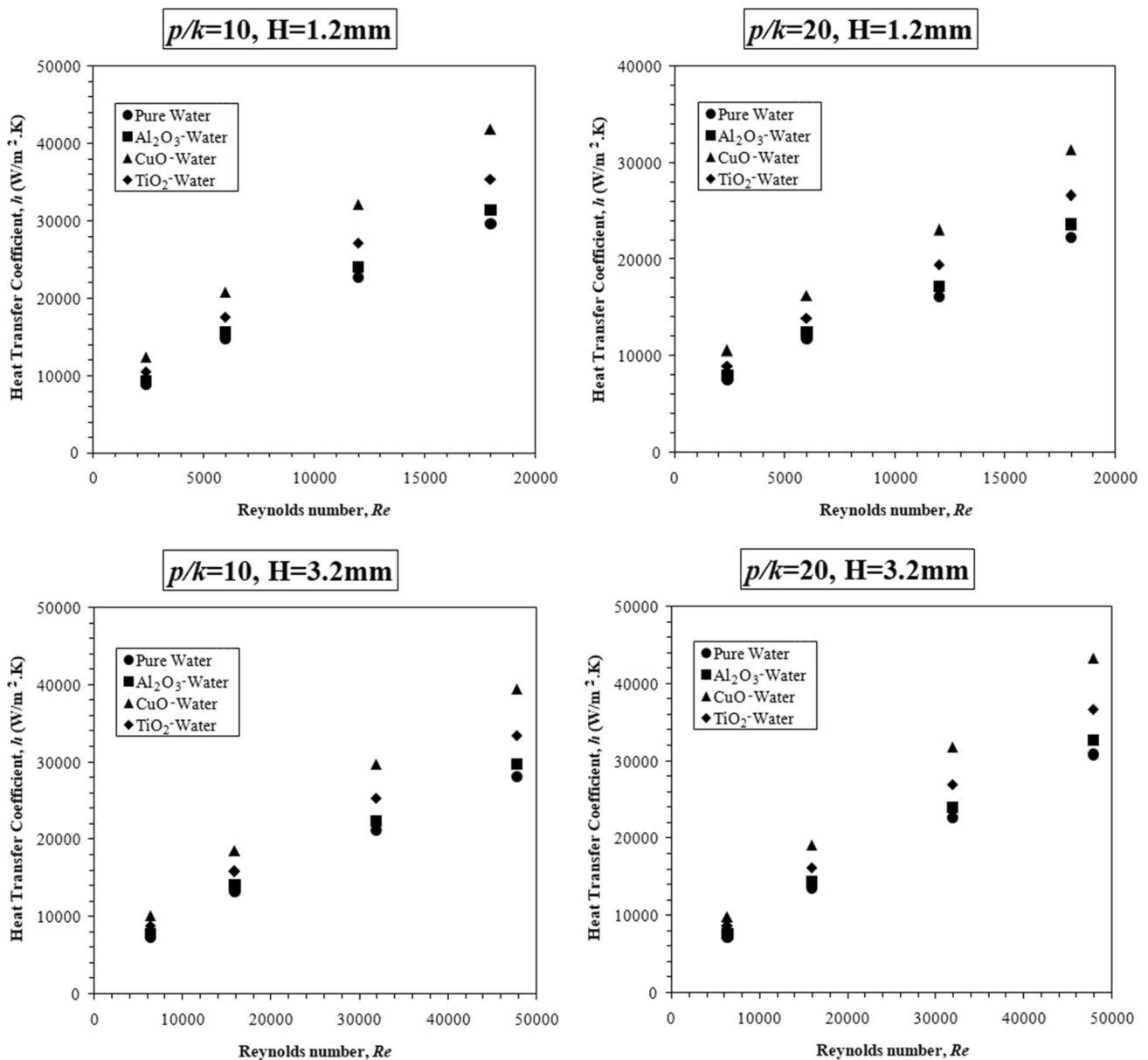


Fig. 16 Comparison of predicted heat transfer coefficients between pure water and t nanofluids

and Nu have been derived using a multivariate nonlinear regression method. From the derived correlations, it has been identified that the relative errors are highly influenced by the values of $C_{\epsilon 1}$ and $C_{\epsilon 2}$ while they are weakly influenced by the values of C_{μ} ($C_{\epsilon 1}$ - $C_{\epsilon 2}$) and σ_k . Thus, calibration of $C_{\epsilon 1}$ and $C_{\epsilon 2}$ has been given the primary importance in this study.

After obtaining the necessary correlations, they have been used as the objective functions in the GA-based

optimization process. The GA-based simulations have been run 10 times for each narrow channel configuration and the mean values of the turbulence model parameters obtained from the trials have been taken as the preliminary calibration values. These values are compared with the combinations from the random sample data having the best fitness values. The comparative study has revealed that the calibration values suggested by GA-based simulations have shown better performance than the random

Table 7 Ratios of Nu for the nanofluids and pure water

Channel configuration	Re	Nu_{nf}/Nu_{pw}		
		Al_2O_3 -water	CuO-water	TiO_2 -water
$p/k=10$; H=1.2 mm	2397.0	1.001	1.326	1.131
	5992.5	1.000	1.336	1.135
	11,985.0	1.001	1.340	1.138
	17,977.5	1.002	1.333	1.135
$p/k=20$; H=1.2 mm	2397.0	1.000	1.312	1.126
	5992.5	1.000	1.299	1.121
	11,985.0	1.004	1.347	1.146
	17,977.5	1.003	1.330	1.137
$p/k=10$; H=3.2 mm	6380.0	1.001	1.300	1.130
	15,950.0	1.001	1.315	1.131
	31,900.0	1.000	1.326	1.140
	47,850.0	1.000	1.327	1.135
$p/k=20$; H=3.2 mm	6380.0	1.001	1.279	1.129
	15,950.0	1.001	1.326	1.132
	31,900.0	1.000	1.324	1.131
	47,850.0	1.000	1.325	1.130

sample combinations for $H=1.2$ mm. The calibrated values of C_{μ} , $C_{\epsilon 1}$, $C_{\epsilon 2}$ and σ_k are 0.01, 1.00, 1.20, and 0.50 respectively for $p/k=10$ and 0.02, 1.00, 1.13, and 0.50 respectively for $p/k=20$. On the other hand, the random sample combinations have shown better performance than the values suggested by GA-based simulations for $H=3.2$ mm. The calibrated values of C_{μ} , $C_{\epsilon 1}$, $C_{\epsilon 2}$ and σ_k are 0.01, 1.09, 1.36, and 0.65 respectively for $p/k=10$ and 0.01, 1.13, 1.48, and 0.83 respectively for $p/k=20$. Once the desired calibrated values are obtained, a validation study is conducted to test the application of the calibrated turbulence model parameters for various flow conditions. For this, further CFD-based simulations with full-scale geometry and varied Re are conducted for both default and calibrated values of the turbulence model parameters. Results reveal that up to 35.83% and 27.30% improvements in the fitness values have been obtained for $p/k=10$ and $p/k=20$ respectively at $H=1.2$ mm and $Re=35,955$. Similarly, up to 15.48% and 18.05% improvements have been obtained for $p/k=10$ and $p/k=20$ respectively at $H=3.2$ mm. Therefore, the calibration process is successful in reducing overall predictive error of the turbulence model.

Finally, an attempt has been made to predict the heat transfer enhancements for the three different nanofluids

using the improved κ - ϵ turbulence model. These nanofluids are Al_2O_3 -water, CuO-water, and TiO_2 -water, all having the same nanoparticle volume fraction of $\phi = 0.02$ and average nanoparticle diameter of 30 nm. Results show that CuO-water nanofluid is predicted to be the best performer among the three, giving almost 1.32 times higher predicted values of Nu from that of pure water with no change in the value of f . On the other hand, Al_2O_3 -water nanofluid and TiO_2 -water nanofluid have around 1.001 and 1.132 higher predicted value of Nu than pure water.

In this study, it has been assumed that ϵ_f and ϵ_{Nu} are functions of C_{μ} , $C_{\epsilon 1}$, $C_{\epsilon 2}$ and σ_k only. However, results indicate that the value of Re also affects ϵ_f and ϵ_{Nu} . Further studies may be conducted to accommodate Re in the correlations for predicting ϵ_f and ϵ_{Nu} . Also, the study may be extended to other narrow channel heights, p/k ratios and other shapes and sizes of the micro-ribs. The effect of bidirectional ribs with both-sided heating may also be studied. Finally, simulated results may be validated with experimental data for nanofluids with the same narrow channel configurations to measure the accuracy and reliability of the improved turbulence model.

Acknowledgements The authors would like to thank University of Dhaka for providing necessary facilities to conduct the research.

Code availability All the MATLAB codes developed in this work are available.

Data availability All the data and material presented in the manuscript are available, authentic and accurate.

Declarations

Conflict of Interest The authors declare that there is no conflict of interest.

Open Access This article is licensed under a Creative Commons Attribution 4.0 International License, which permits use, sharing, adaptation, distribution and reproduction in any medium or format, as long as you give appropriate credit to the original author(s) and the source, provide a link to the Creative Commons licence, and indicate if changes were made. The images or other third party material in this article are included in the article's Creative Commons licence, unless indicated otherwise in a credit line to the material. If material is not included in the article's Creative Commons licence and your intended use is not permitted by statutory regulation or exceeds the permitted use, you will need to obtain permission directly from the copyright holder. To view a copy of this licence, visit <http://creativecommons.org/licenses/by/4.0/>.

Appendix 1

Table 8 Effect of crossover rate on GA-based simulation results for mutation rate 0.05 and channel configuration $p/k = 10$, $H = 1.2$ mm.

Trial #	Crossover rate: 0.50				Crossover rate: 0.70				Crossover rate: 0.90			
	C_{μ}	$C_{\epsilon 1}$	$C_{\epsilon 2}$	σ_k	C_{μ}	$C_{\epsilon 1}$	$C_{\epsilon 2}$	σ_k	C_{μ}	$C_{\epsilon 1}$	$C_{\epsilon 2}$	σ_k
1	0.01	1.00	1.19	0.50	0.01	1.00	1.21	0.50	0.03	1.00	1.19	0.50
2	0.01	1.01	1.21	0.50	0.02	1.01	1.19	0.50	0.01	1.00	1.20	0.50
3	0.01	1.00	1.19	0.50	0.01	1.00	1.19	0.50	0.01	1.00	1.20	0.50
4	0.01	1.01	1.19	0.50	0.02	1.01	1.19	0.50	0.01	1.01	1.21	0.50
5	0.01	1.01	1.20	0.50	0.01	1.01	1.21	0.50	0.02	1.00	1.20	0.50
6	0.01	1.00	1.20	0.50	0.01	1.00	1.20	0.50	0.01	1.01	1.19	0.50
7	0.02	1.00	1.19	0.50	0.01	1.00	1.20	0.50	0.01	1.01	1.19	0.50
8	0.02	1.00	1.20	0.50	0.01	1.00	1.19	0.50	0.01	1.00	1.19	0.50
9	0.01	1.01	1.20	0.50	0.01	1.01	1.20	0.50	0.01	1.01	1.21	0.50
10	0.01	1.00	1.19	0.50	0.01	1.00	1.21	0.50	0.01	1.00	1.19	0.50
Mean	0.01	1.00	1.20	0.50	0.01	1.00	1.20	0.50	0.01	1.00	1.20	0.50
SD	0.00	0.01	0.01	0.00	0.00	0.01	0.01	0.00	0.01	0.01	0.01	0.00

Table 9 Effect of mutation rate on GA-based simulation results for crossover rate 0.50 and channel configuration $p/k = 10$, $H = 1.2$ mm.

Trial #	Mutation rate: 0.01				Crossover rate: 1.00			
	C_{μ}	$C_{\epsilon 1}$	$C_{\epsilon 2}$	σ_k	C_{μ}	$C_{\epsilon 1}$	$C_{\epsilon 2}$	σ_k
1	0.01	1.00	1.20	0.50	0.02	1.00	1.21	0.50
2	0.01	1.00	1.20	0.50	0.01	1.01	1.20	0.50
3	0.02	1.00	1.20	0.50	0.01	1.00	1.21	0.50
4	0.01	1.00	1.20	0.50	0.02	1.00	1.20	0.50
5	0.01	1.00	1.20	0.50	0.01	1.00	1.19	0.50
6	0.01	1.00	1.21	0.50	0.02	1.02	1.19	0.50
7	0.01	1.01	1.19	0.50	0.01	1.00	1.20	0.50
8	0.01	1.00	1.20	0.50	0.02	1.00	1.20	0.50
9	0.02	1.00	1.20	0.50	0.01	1.00	1.20	0.50
10	0.01	1.00	1.20	0.50	0.01	1.01	1.21	0.50
Mean	0.01	1.00	1.20	0.50	0.01	1.00	1.20	0.50
SD	0.01	0.00	0.00	0.00	0.01	0.01	0.01	0.00

Table 10 Calibrated values of turbulence model parameters obtained from GA-based simulations with 0.5 crossover and mutation rates 0.5 and 0.05 respectively.

Trial #	$p/k = 10, H = 3.2$ mm				$p/k = 20, H = 1.2$ mm				$p/k = 20, H = 3.2$ mm			
	C_{μ}	$C_{\epsilon 1}$	$C_{\epsilon 2}$	σ_k	C_{μ}	$C_{\epsilon 1}$	$C_{\epsilon 2}$	σ_k	C_{μ}	$C_{\epsilon 1}$	$C_{\epsilon 2}$	σ_k
1	0.01	1.00	1.23	0.50	0.01	1.00	1.13	0.50	0.01	1.50	1.77	0.50
2	0.03	1.00	1.22	0.50	0.01	1.00	1.13	0.50	0.01	1.50	1.76	0.50
3	0.01	1.00	1.22	0.50	0.01	1.00	1.12	0.50	0.01	1.50	1.78	0.50
4	0.02	1.00	1.22	0.50	0.03	1.00	1.12	0.50	0.03	1.50	1.78	0.50
5	0.02	1.00	1.23	0.50	0.01	1.00	1.12	0.50	0.01	1.50	1.78	0.50
6	0.01	1.00	1.23	0.50	0.01	1.00	1.13	0.50	0.02	1.50	1.77	0.50

Trial #	$p/k=10, H=3.2 \text{ mm}$				$p/k=20, H=1.2 \text{ mm}$				$p/k=20, H=3.2 \text{ mm}$			
	C_μ	$C_{\epsilon 1}$	$C_{\epsilon 2}$	σ_k	C_μ	$C_{\epsilon 1}$	$C_{\epsilon 2}$	σ_k	C_μ	$C_{\epsilon 1}$	$C_{\epsilon 2}$	σ_k
7	0.02	1.00	1.22	0.50	0.01	1.00	1.13	0.50	0.02	1.50	1.77	0.50
8	0.02	1.00	1.22	0.50	0.03	1.00	1.13	0.50	0.01	1.50	1.77	0.50
9	0.02	1.00	1.22	0.50	0.03	1.00	1.13	0.50	0.01	1.50	1.77	0.50
10	0.03	1.00	1.22	0.50	0.01	1.00	1.12	0.50	0.02	1.50	1.78	0.50
Mean	0.02	1.00	1.22	0.50	0.02	1.00	1.13	0.50	0.02	1.50	1.77	0.50
SD	0.01	0.00	0.00	0.00	0.01	0.00	0.01	0.00	0.01	0.00	0.01	0.00

References:

- Kadam ST, Kumar R (2014) Twenty first century cooling solution: microchannel heat sinks. *Int J Therm Sci* 85:73–92. <https://doi.org/10.1016/j.ijthermalsci.2014.06.013>
- Han JC et al (1989) Augmented heat transfer in rectangular channels of narrow aspect ratios with rib turbulators. *Int J Heat Mass Transf* 32(9):1619–1630. [https://doi.org/10.1016/0017-9310\(89\)90044-6](https://doi.org/10.1016/0017-9310(89)90044-6)
- Islam SM et al (1998) Experimental study on heat transfer augmentation for high heat flux removal in rib-roughened narrow channels. *J nucl sci technol* 35(9):671–678. <https://doi.org/10.1080/18811248.1998.9733923>
- Islam SM et al (2002) Experimental analysis of turbulent flow structure in a fully developed rib-roughened rectangular channel with PIV. *Exp Fluid* 33(2):296–306. <https://doi.org/10.1007/s00348-002-0432-9>
- Islam SM et al (2009) Prediction of turbulent flow structure in a fully developed rib-roughened narrow rectangular channel. *J Therm Sci* 18(2):126–136. <https://doi.org/10.1007/s11630-009-0126-1>
- Chang SW, Liou TM, Ming Hsin Lu (2005) Heat transfer of rectangular narrow channel with two opposite scale-roughened walls. *Int J Heat Mass Transf* 48(19–20):3921–3931. <https://doi.org/10.1016/j.ijheatmasstransfer.2005.04.015>
- Chang SW et al (2005) Heat transfer in a twin-blow narrow channel with two opposite walls roughened by skewed ribs arranged in staggered manner. *Int j therm sci* 44(7):694–708. <https://doi.org/10.1016/j.ijthermalsci.2004.05.005>
- Esmaili Q, Ranjbar AA, Porkhial S (2018) Experimental analysis of heat transfer in ribbed microchannel. *Int J Therm Sci* 130:140–147. <https://doi.org/10.1016/j.ijthermalsci.2018.04.020>
- Ma C et al (2018) Comparative study of convective heat transfer performance of steam and air flow in rib roughened channels. *J Therm Sci* 27(2):184–194. <https://doi.org/10.1007/s11630-018-0999-y>
- Moon M-A, Park M-J, Kim K-Y (2014) Evaluation of heat transfer performances of various rib shapes. *Int J Heat Mass Transf* 71:275–284. <https://doi.org/10.1016/j.ijheatmasstransfer.2013.12.026>
- Mereu R, Lampitella P, Inzoli F (2014) Preliminary fluid dynamic analysis of turbulent flat and ribbed square duct via CFD approach. In: *ASME 2014 4th Joint US-European fluids engineering division summer meeting collocated with the ASME 2014 12th international conference on nanochannels, microchannels, and minichannels*. American society of mechanical engineers digital collection, DOI: <https://doi.org/10.1115/FEDSM2014-22088>
- Khan AA, Kim SM, Kim KY (2016) Performance analysis of a micro-channel heat sink with various rib configurations. *J Thermophys Heat Transf* 30(4):782–790. <https://doi.org/10.2514/1.T4663>
- Moon M-A, Kim K-Y (2016) Exergetic analysis for optimization of a rotating equilateral triangular cooling channel with staggered square ribs. *Int J Fluid Mach Syst* 9(3):229–236. <https://doi.org/10.5293/IJFMS.2016.9.3.229>
- Khalid A, Xie G, Sundén B (2016) Numerical simulations of flow structure and turbulent heat transfer in a square ribbed channel with varying rib pitch ratio. *J Enhanc Heat Transf*. <https://doi.org/10.1615/JEnhHeatTransf.2017018645>
- Pope SB (2000) *Turbulent flows*, 1st edn. Cambridge University Press, UK
- Shaukat Ali Md, Tariq Andallib, Gandhi BK (2016) Role of chamfering angles and flow through slit on heat transfer augmentation behind a surface-mounted rib. *J Heat Transf DOI* 10(1115/1):4033747
- Seo J-W, Afzal A, Kim K-Y (2016) Efficient multi-objective optimization of a boot-shaped rib in a cooling channel. *Int J Therm Sci* 106:122–133. <https://doi.org/10.1016/j.ijthermalsci.2016.03.015>
- Popov IA, Skrypnik AN, Schelchikov AV (2019) Hydraulic resistance and heat transfer augmentation in pipes with inner helical micro-ribs: review, data generalisation, and technical recommendations. *J Phys Conf Seri* 1369(1):012064. <https://doi.org/10.1088/1742-6596/1369/1/012064>
- Wang G, Qian N, Ding G (2019) Heat transfer enhancement in microchannel heat sink with bidirectional rib. *Int J Heat Mass Transf* 136:597–609. <https://doi.org/10.1016/j.ijheatmasstransfer.2019.02.018>
- Li J et al (2019) Experimental investigation of the heat transfer and flow characteristics of microchannels with microribs. *Int J Heat Mass Transf* 143:118482. <https://doi.org/10.1016/j.ijheatmasstransfer.2019.118482>
- Fadhil D, Al-Turaihi R, Abed A (2019) Effect of semi-circle rib on heat transfer coefficient in a rectangular channel. *Front Heat Mass Transf (FHMT)*. <https://doi.org/10.5098/hmt.13.29>
- Ali MS, Sharma N, Tariq A (2019) Heat transfer and flow field features between surface mounted trapezoidal-ribs. *J Mech Sci Technol* 33(10):5017–5023. <https://doi.org/10.1007/s12206-019-0940-7>
- Li H et al (2020) Experimental investigation of turbulent flow in a rotating straight channel with continuous ribs. *Phys Fluid* 32(1):015114. <https://doi.org/10.1063/1.5131223>
- Akbari OA et al (2016) "Investigation of rib's height effect on heat transfer and flow parameters of laminar water–Al₂O₃ nanofluid in a rib-microchannel. *Appl Math Comput* 290:135–153. <https://doi.org/10.1016/j.amc.2016.05.053>
- Alipour H et al (2017) Influence of T-semi attached rib on turbulent flow and heat transfer parameters of a silver-water nanofluid with different volume fractions in a three-dimensional trapezoidal microchannel. *Phys E Low-Dimens Syst Nanostructures* 88:60–76. <https://doi.org/10.1016/j.physe.2016.11.021>
- Behnampour A et al (2017) Analysis of heat transfer and nanofluid flow in microchannels with trapezoidal, rectangular and triangular shaped ribs. *Phys E Low-Dimens Syst Nanostructures* 91:15–31. <https://doi.org/10.1016/j.physe.2017.04.006>

27. Gravndyan Q et al (2017) The effect of aspect ratios of rib on the heat transfer and laminar water/TiO₂ nanofluid flow in a two-dimensional rectangular microchannel. *J Mol Liq* 236:254–265. <https://doi.org/10.1016/j.molliq.2017.04.030>
28. Shamsi MR et al (2017) Increasing heat transfer of non-newtonian nanofluid in rectangular microchannel with triangular ribs. *Phys E Low-Dimens Syst Nanostructures* 93:167–178. <https://doi.org/10.1016/j.physe.2017.06.015>
29. Gholami MR et al (2018) The effect of rib shape on the behavior of laminar flow of oil/MWCNT nanofluid in a rectangular microchannel. *J Therm Anal Calorim* 134(3):1611–1628. <https://doi.org/10.1007/s10973-017-6902-3>
30. Parsaiemehr M et al (2018) Turbulent flow and heat transfer of water/Al₂O₃ nanofluid inside a rectangular ribbed channel. *Phys E Low-Dimens Syst Nanostructures* 96:73–84. <https://doi.org/10.1016/j.physe.2017.10.012>
31. Cheloi NA, Akbari OA, Toghraie D (2019) Computational fluid dynamics and laminar heat transfer of water/Cu nanofluid in ribbed microchannel with a two-phase approach. *Int J Numer Method Heat Fluid Flow*. <https://doi.org/10.1108/HFF-05-2018-0243>
32. Pahlevaninejad N, Rahimi M, Gorzin M (2020) Thermal and hydrodynamic analysis of non-newtonian nanofluid in wavy microchannel. *J Therm Anal Calorim*. <https://doi.org/10.1007/s10973-019-09229-x>
33. Rocha PC et al (2014) k- ω SST (shear stress transport) turbulence model calibration: a case study on a small scale horizontal axis wind turbine. *Energy* 65:412–418. <https://doi.org/10.1016/j.energy.2013.11.050>
34. Rocha PC et al (2016) A case study on the calibration of the k- ω SST (shear stress transport) turbulence model for small scale wind turbines designed with cambered and symmetrical airfoils. *Energy* 97:144–150. <https://doi.org/10.1016/j.energy.2015.12.081>
35. Guillas S, Glover N, Malki-Epshtein L (2014) Bayesian calibration of the constants of the k- ϵ turbulence model for a CFD model of street canyon flow. *Comput Method Appl Mech Eng* 279:536–553. <https://doi.org/10.1016/j.cma.2014.06.008>
36. Matyushenko AA, Garbaruk AV (2016) Adjustment of the k- ω SST turbulence model for prediction of airfoil characteristics near stall. *J Phys Conf Series*. <https://doi.org/10.1088/1742-6596/769/1/012082>
37. DeChant LJ et al (2017) k- ϵ Turbulence Model Parameter Estimates Using an Approximate Self-similar Jet-in-Crossflow Solution. In: *8th AIAA theoretical fluid mechanics conference*. DOI: <https://doi.org/10.2514/6.2017-4167>
38. Shirzadi M, Mirzaei PA, Naghashzadegan M (2017) Improvement of k-epsilon turbulence model for CFD simulation of atmospheric boundary layer around a high-rise building using stochastic optimization and Monte Carlo Sampling technique. *J Wind Eng Ind Aerodyn* 171:366–379. <https://doi.org/10.1016/j.jweia.2017.10.005>
39. Liu C, Weiyang Bu, Dong Xu (2017) Multi-objective shape optimization of a plate-fin heat exchanger using CFD and multi-objective genetic algorithm. *Int J Heat Mass Transf* 111:65–82. <https://doi.org/10.1016/j.ijheatmasstransfer.2017.03.066>
40. Na J et al (2017) Multi-objective optimization of microchannel reactor for fischer-tropsch synthesis using computational fluid dynamics and genetic algorithm. *Chem Eng J* 313:1521–1534. <https://doi.org/10.1016/j.cej.2016.11.040>
41. Ghorbani B et al (2017) CFD modeling and optimization of a latent heat storage unit for running a solar assisted single effect Li-Br absorption chiller using multi-objective genetic algorithm. *Sustain cities soc* 34:321–334. <https://doi.org/10.1016/j.scs.2017.05.023>
42. Daróczy L, Janiga G, Thévenin D (2018) Computational fluid dynamics based shape optimization of airfoil geometry for an H-rotor using a genetic algorithm. *Eng Optim* 50(9):1483–1499. <https://doi.org/10.1080/0305215X.2017.1409350>
43. Prieler R et al (2018) CFD-based optimization of a transient heating process in a natural gas fired furnace using neural networks and genetic algorithms. *Appl Therm Eng* 138:217–234. <https://doi.org/10.1016/j.applthermaleng.2018.03.042>
44. Oh JT, Chien NB (2018) Optimization design by coupling computational fluid dynamics and genetic algorithm. *Comput Fluid Dyn Basic Instrum Appl Sci*. <https://doi.org/10.5772/intechopen.72316>
45. Sun X, Yoon JY (2018) Multi-objective optimization of a gas cyclone separator using genetic algorithm and computational fluid dynamics. *Powder Technol* 325:347–360. <https://doi.org/10.1016/j.powtec.2017.11.012>
46. Pourfatah F et al (2020) On the optimization of a vertical twisted tape arrangement in a channel subjected to MWCNT-water nanofluid by coupling numerical simulation and genetic algorithm. *J Therm Anal Calorim*. <https://doi.org/10.1007/s10973-020-09490-5>
47. Dittus FW, Boelter LMK (1930) Publications on engineering, vol 2. University of California at Berkeley, Berkeley CA, pp 443–461
48. Maïga SEB et al (2004) Heat transfer behaviours of nanofluids in a uniformly heated tube. *Superlattices Microstruct* 35(3–6):543–557. <https://doi.org/10.1016/j.spmi.2003.09.012>
49. Akbari M, Galanis N, Behzadmehr A (2012) Comparative assessment of single and two-phase models for numerical studies of nanofluid turbulent forced convection. *Int J Heat Fluid Flow* 37:136–146. <https://doi.org/10.1016/j.ijheatfluidflow.2012.05.005>
50. Bianco V et al (2009) Numerical investigation of nanofluids forced convection in circular tubes. *Appl Therm Eng* 29(17–18):3632–3642. <https://doi.org/10.1016/j.applthermaleng.2009.06.019>
51. Rostamani M et al (2010) Numerical study of turbulent forced convection flow of nanofluids in a long horizontal duct considering variable properties. *Int Commun Heat Mass Transf* 37(10):1426–1431. <https://doi.org/10.1016/j.icheatmasstransfer.2010.08.007>
52. Buongiorno J (2006) Convective transport in nanofluids. *J Heat Transf* 128(3):240–250. <https://doi.org/10.1115/1.2150834>
53. Behroyan I et al (2015) Turbulent forced convection of Cu-water nanofluid: CFD model comparison. *Int Commun Heat Mass Transf* 67:163–172. <https://doi.org/10.1016/j.icheatmasstransfer.2015.07.014>
54. Gupta S, Kumar D, Singh J (2018) MHD mixed convective stagnation point flow and heat transfer of an incompressible nanofluid over an inclined stretching sheet with chemical reaction and radiation. *Int J Heat Mass Transf* 118:378–387. <https://doi.org/10.1016/j.ijheatmasstransfer.2017.11.007>
55. Maxwell JC (1873) A treatise on electricity and magnetism, vol 1. Clarendon Press, Oxford
56. Kamyar A, Saidur R, Hasanuzzaman M (2012) Application of computational fluid dynamics (CFD) for nanofluids. *Int J Heat Mass Transf* 55(15–16):4104–4115
57. Launder BE, Spalding DB (1983) The numerical computation of turbulent flows. Numer predict flow heat transf turbul combust. <https://doi.org/10.1016/B978-0-08-030937-8.50016-7>
58. Von Kármán, Theodore.(1931) *Mechanical similitude and turbulence*. No. 611. National advisory committee for aeronautics
59. Neuman SP (1977) Theoretical derivation of Darcy's law. *Act Mech* 25(3–4):153–170. <https://doi.org/10.1007/BF01376989>

Publisher's Note Springer Nature remains neutral with regard to jurisdictional claims in published maps and institutional affiliations.